Signatures of vibronic coupling in two-dimensional electronic-vibrational and vibrational-electronic spectroscopies

James D. Gaynor, and Munira Khalil

Citation: The Journal of Chemical Physics **147**, 094202 (2017); doi: 10.1063/1.4991745
View online: https://doi.org/10.1063/1.4991745
View Table of Contents: http://aip.scitation.org/toc/jcp/147/9
Published by the American Institute of Physics

Signatures of vibronic coupling in two-dimensional electronic-vibrational and vibrational-electronic spectroscopies

James D. Gaynor and Munira Khalil[a)]
Department of Chemistry, University of Washington, P.O. Box 351700, Seattle, Washington 98195, USA

(Received 22 June 2017; accepted 10 August 2017; published online 1 September 2017)

Two-Dimensional Electronic-Vibrational (2D EV) spectroscopy and Two-Dimensional Vibrational-Electronic (2D VE) spectroscopy are new coherent four-wave mixing spectroscopies that utilize both electronically resonant and vibrationally resonant field-matter interactions to elucidate couplings between electronic and vibrational degrees of freedom. A system Hamiltonian is developed here to lay a foundation for interpreting the 2D EV and 2D VE signals that arise from a vibronically coupled molecular system in the condensed phase. A molecular system consisting of one anharmonic vibration and two electronic states is modeled. Equilibrium displacement of the vibrational coordinate and vibrational frequency shifts upon excitation to the first electronic excited state are included in our Hamiltonian through linear and quadratic vibronic coupling terms. We explicitly consider the nuclear dependence of the electronic transition dipole moment and demonstrate that these spectroscopies are sensitive to non-Condon effects. A series of simulations of 2D EV and 2D VE spectra obtained by varying parameters of the system, system-bath, and interaction Hamiltonians demonstrate that one of the following conditions must be met to observe signals: (1) non-zero linear and/or quadratic vibronic coupling in the electronic excited state, (2) vibrational-coordinate dependence of the electronic transition dipole moment, or (3) electronic-state-dependent vibrational dephasing dynamics. We explore how these vibronic interactions are manifested in the positions, amplitudes, and line shapes of the peaks in 2D EV and 2D VE spectroscopies. *Published by AIP Publishing.* [http://dx.doi.org/10.1063/1.4991745]

I. INTRODUCTION

The coupled motions of electronic and vibrational degrees of freedom, generally referred to as vibronic couplings, play an important role in energy and charge transfer processes. There is an increasing interest to directly measure and compute these vibronic couplings in complex disordered condensed phase systems and eventually harness them to control chemical and biophysical photo-induced energy conversion processes.[1] In recent years, several two-dimensional electronic spectroscopy (2D ES) studies have revealed vibronic coherence in natural and artificial light-harvesting systems.[2–10] There has also been theoretical and experimental interest in understanding the role of vibronic couplings in proton-coupled electron transfer processes.[11–15] Two-dimensional IR (2D IR) spectroscopy and 2D ES have become established experimental tools for interrogating vibrational and electronic dynamics, respectively, in complex systems. Over the last two decades, experimental and theoretical strategies have been developed to obtain microscopic information from analyzing the time-dependent positions, amplitudes, and line shapes of the various peaks in 2D IR and 2D electronic spectra. To address the issue of experimental measurement of vibronic phenomena, 2D Electronic-Vibrational (EV) spectroscopy[16] and 2D Vibrational-Electronic (VE) spectroscopy[17] have been recently developed. These third order nonlinear spectroscopies employ electronically and vibrationally resonant excitation and probe fields to directly interrogate inter- and intramolecular vibronic couplings in molecular systems. For example, using 2D VE spectroscopy, mode-dependent vibronic coupling strengths have been determined in a transition metal mixed valence compound, and local vibrations have been used to track electronic energy flow among various pigments in a light harvesting complex using 2D EV spectroscopy.[17–19] Technical developments have extended the range of accessible molecular phenomena by incorporating UV and octave-spanning mid-IR pulses into the 2D EV experiment.[20] As the 2D EV and 2D VE experimental studies and their interpretation continue to expand and develop,[21–23] it is important to develop an intuitive understanding of how molecular vibronic couplings are encoded in the 2D spectra.

To this end, a system Hamiltonian is introduced in this paper that describes a single anharmonic vibration in the ground electronic state that has linear and quadratic vibronic coupling in the excited electronic state. This Hamiltonian is used in simulating 2D EV and 2D VE spectra of systems that have varying degrees of intramolecular vibronic coupling. This formulation parallels the Herzberg-Teller adiabatic approximation[24] by including a linear dependence of nuclear coordinates on the electronic transition dipole moment. It is shown that the extent of vibronic coupling is reflected in the peak positions, the nuclear dependence of the electronic transition contributes to the peak amplitudes, and

a) Author to whom correspondence should be addressed: mkhalil@uw.edu

electronic-state-dependent vibrational dephasing affects peak line shapes in 2D EV and 2D VE spectra. Selection rules for these 2D spectroscopies are described through systematic simulations of 2D spectra. This paper is organized as follows: Sec. II develops the vibronic Hamiltonian and the interaction Hamiltonian; Sec. III categorizes all contributing 2D EV and 2D VE signals under consideration and characterizes the peak positions, amplitudes, and line shapes for both techniques; Sec. IV discusses simulations for cases of systematically varied degrees of vibronic coupling; Sec. V summarizes the 2D EV and 2D VE selection rules elucidated through the simulations; and Sec. VI discusses additional signals accessible with different input pulse parameters, polarization-selective signals, and future directions.

II. VIBRONIC MATERIAL AND INTERACTION HAMILTONIANS

A theoretical description of a molecular system under study with nonlinear spectroscopic methods begins with a quantum mechanical material Hamiltonian to describe the molecular system and an interaction Hamiltonian to describe the coupling between the external light fields and the system. The material Hamiltonian is the sum of individual Hamiltonians for the system, the bath, and the system-bath interaction. To model the simplest case for 2D EV and 2D VE spectroscopies of systems with vibronic coupling, we use a Hamiltonian, $H_{vibronic}$, that describes a single local vibrational mode and two electronic states: the ground state, $|g\rangle$, and the first excited state, $|e\rangle$. Many treatments of molecular vibronic couplings exist.[25–31] The vibronic system Hamiltonian described by Tonks and Page[30] models equilibrium position displacement, frequency shifting, and vibrational mode mixing (known as the Duschinsky rotation[32]) upon electronic excitation. In this formulation, the excited state Hamiltonian includes the effects of excited state equilibrium displacement through a linear vibronic coupling term and the frequency shifting and Duschinsky rotation are included with quadratic vibronic coupling terms.[30,33] More recently, Vallet *et al.*[34] used this model to derive analytical expressions for simulating doubly resonant IR-visible sum frequency generation spectra for surface adsorbed molecules with harmonic potentials. We introduce cubic anharmonicity to this vibronic Hamiltonian and use it to describe a single anharmonic vibration in the ground electronic state that has linear and quadratic vibronic coupling in the excited electronic state.

The vibronic Hamiltonian is defined as the sum of the ground and excited state Hamiltonians, $H_{vibronic} = H_g + H_e$. The electronic ground state Hamiltonian, H_g, has the following form:

$$H_g = \frac{P_j^2}{2m_j} + V_g(Q_j), \tag{1}$$

$$V_g(Q_j) = \frac{1}{2}\hbar\omega_j^0 Q_j^2 + \frac{1}{6}\hbar\omega_j^0 g_{jjj} Q_j^3. \tag{2}$$

In the above equations, $Q_j = \sqrt{\frac{m_j\omega_j^0}{\hbar}}q_j$ is the reduced vibrational coordinate for the jth vibrational coordinate (q_j), m_j is the reduced mass, ω_j^0 is the natural oscillator frequency, and P_j is the momentum operator. The vibrational coordinate could be either a local mode or a normal mode, depending on the molecular problem of interest. The ground state potential $[V_g(Q_j)]$ for the jth vibration in Eq. (2) is obtained by the Taylor expansion of the harmonic potential to include the cubic terms.[35,36] The cubic expansion coefficient, g_{ijk}, is dimensionless and related to the third order derivative of $V_g(Q_j)$ evaluated at the equilibrium position. In this particular case, $i = j = k$ because only one vibrational mode is being considered. The excited electronic state Hamiltonian, H_e, is written as H_g raised in energy by the electronic energy gap and includes vibronic coupling to the first and second order in the vibrational coordinate of the excited state potential, $V_e(Q_j)$,

$$H_e = \frac{P_j^2}{2m_j} + V_e(Q_j), \tag{3}$$

$$V_e(Q_j) = V_g(Q_j) + \hbar\omega_{eg}^0 + \hbar\omega_j^0 \mathrm{V}_j^{(1)} Q_j + \frac{1}{2}\hbar\omega_j^0 \mathrm{V}_{j,j}^{(2)} Q_j^2. \tag{4}$$

The electronic transition frequency between the lowest vibrational levels of the harmonic ground and excited electronic states is given by ω_{eg}^0. The dimensionless vibronic coupling coefficient, $\mathrm{V}_j^{(1)}$, reflects the linear coupling strength of the jth vibration to the electronic transition and results in the equilibrium position displacement of the vibrational mode upon electronic excitation. The dimensionless quadratic vibronic coupling coefficient, $\mathrm{V}_{j,j}^{(2)}$, is responsible for the frequency shifting of the jth vibrational mode in the electronic excited state. When a system with two anharmonic vibrations is considered, both frequency shifting ($\mathrm{V}_{j,j}^{(2)}$) and vibrational mode mixing ($\mathrm{V}_{j,k}^{(2)}$) arise from quadratic vibronic coupling. The linear and quadratic vibronic coupling coefficients are related to the first and second order derivatives of the excited state potential with respect to the vibrational coordinate, respectively.

The material Hamiltonian consists of the vibronic system described above, a bath, and the system-bath interactions. In the context of a solute-solvent molecular system, the "bath" can represent the solvent and all the remaining solute degrees of freedom not described in the system Hamiltonian. The system-bath interaction can lead to shifts in vibronic transition frequencies, electronic and vibrational relaxation dynamics, and reorientational dynamics. For this work, we use the approach of Sung and Silbey[37] to describe the bath and system-bath Hamiltonians (H_B and H_{SB}). Briefly, the bath consists of harmonic oscillators and the system-bath interaction is linear in the bath coordinates, q_B. The system-bath interaction is included by diagonalizing $H_{vibronic}$ and coupling the eigenstates to the bath through H_{SB}. Here, H_{SB} is diagonal in the system eigenstate basis, and it reflects the fluctuations of the vibronic frequencies.[37] The pure dephasing effects of system-bath interactions are considered here and incorporated through energy gap correlation functions. As shown in Secs. III A 3, III B 3, and IV, we include electronic dephasing, vibrational dephasing, and electronic-state-dependent vibrational dephasing of the vibronic states and explore how these microscopic effects are observed in 2D EV and VE spectra.

The interaction between an external radiation field [$\mathbf{E}(k,\omega,t)$] and the vibronic system described earlier is encoded in the interaction Hamiltonian, H_{int},

$$\begin{aligned} H_{int} &= -\mathbf{M}\cdot\mathbf{E}(k,\omega,t) \\ &= -\sum_a\sum_b |a\rangle\,\mu^{a,b}\cdot\mathbf{E}(k,\omega,t)\,\langle b|, \end{aligned} \tag{5}$$

where the system dipole operator is given by $\mathbf{M}$ and the transition dipole matrix elements are denoted by $\mu^{a,b}$. In the above equation, $|a\rangle$ and $|b\rangle$ correspond to the vibronic system eigenstates of $H_{vibronic}$ described above, and they are indexed by their electronic state and vibrational state. We denote an eigenstate of the ground electronic manifold (g) with vibrational quanta ($v = 0, 1, \ldots, n$) as $|g, v\rangle$ and an eigenstate of the excited electronic manifold (e) with vibrational quanta ($v' = 0', 1', \cdots, n'$) as $|e, v'\rangle$. In general, the transition moment between the vibronic states $|a\rangle$ and $|b\rangle$ is defined as

$$\mu^{a,b} = \langle a(r,Q)|\,\mathbf{M}\,|b(r,Q)\rangle\,, \tag{6}$$

where the vibronic states depend on both the electronic coordinates, r, and the reduced vibrational coordinates, Q. The eigenstates are written as Born-Oppenheimer adiabatic eigenstates[38] and expressed as the products of the electronic wave function, $\psi(r,Q)$, and the nuclear wave function, $\chi(Q)$,

$$\begin{aligned} |a(r,Q)\rangle &= |\psi^a(r,Q)\rangle\,|\chi^a(Q)\rangle\,, \\ |b(r,Q)\rangle &= |\psi^b(r,Q)\rangle|\chi^b(Q)\rangle, \end{aligned} \tag{7}$$

where superscripts a and b specify wave functions in $|a\rangle$ and $|b\rangle$. The vibronic eigenstates defined in Eq. (7) fit within the "Born representation" defined by Ballhausen and Hansen.[39] They can be considered eigenfunctions of a dynamical Schrödinger equation in a basis set that spans a complete electronic space for each value of Q.

The transition dipole operator can be written as the sum of individual operators for the electronic and vibrational coordinates, $\mathbf{M} = \mathbf{M}_{elec}(r)+\mathbf{M}_{vib}(Q)$.[40–42] By rewriting Eq. (6) using this expression for $\mathbf{M}$ and the Born-Oppenheimer adiabatic wave functions in Eq. (7), the transition dipole moment $\mu^{a,b}$ explicitly includes both electronic and vibrational transitions in the system,[40,42]

$$\begin{aligned} \mu^{a,b} = &\left\langle\psi^a(r,Q)\middle|\psi^b(r,Q)\right\rangle\left\langle\chi^a(Q)\middle|\mathbf{M}_{vib}(Q)\middle|\chi^b(Q)\right\rangle \\ &+\left\langle\chi^a(Q)\middle|\chi^b(Q)\right\rangle\left\langle\psi^a(r,Q)\middle|\mathbf{M}_{elec}(r)\middle|\psi^b(r,Q)\right\rangle. \end{aligned} \tag{8}$$

When a vibronic transition between electronic states occurs (i.e., $|g, v\rangle \rightarrow |e, v'\rangle$), the electronic overlap integral in the first term on the right-hand side of Eq. (8) vanishes and $\mu^{a,b}$ reduces to the electronic transition dipole multiplied by the appropriate vibrational overlap integral. The nuclear dependence of the electronic transition dipole moment is included by letting $\mathbf{M}_{elec}(r) \cong \mathbf{M}_{eg}(Q)$ where $\mathbf{M}_{eg}(Q)$ is the electronic transition dipole operator in terms of Q. The Q dependence is made explicit by Taylor expanding $\mathbf{M}_{eg}(Q)$ over the vibrational coordinate about the equilibrium nuclear configuration, Q_0,

$$\mathbf{M}_{eg}(Q) = \mu_{eg}^{(0)} + \sum_j \mu_{eg}^{(1)}Q_j + \frac{1}{2}\sum_{j,k}\mu_{eg}^{(2)}Q_jQ_k + \cdots, \tag{9}$$

with the expansion coefficients given by $\mu_{eg}^{(0)} = \mathbf{M}_{eg}(Q_0)$, $\mu_{eg}^{(1)} = \left(\frac{\partial\mathbf{M}_{eg}}{\partial Q_j}\right)_{Q_0}$, and $\mu_{eg}^{(2)} = \left(\frac{\partial^2\mathbf{M}_{eg}}{\partial Q_j\partial Q_k}\right)_{Q_0}$. The Condon approximation breaks down when the linear and higher order terms in $\mathbf{M}_{eg}$ are non-negligible. We include the nuclear dependence of the electronic transition in our approach, allowing for these non-Condon effects to be considered in the vibronic systems of interest. Our treatment parallels the Herzberg-Teller adiabatic approximation,[24,39,42–45] which includes a linear nuclear coordinate dependence of the electronic transition moment through the first order term in the expansion of the transition dipole moment. The first order terms are referred to as Herzberg-Teller vibronic coupling terms. In our formulation of the transition dipole moment, we include the Herzberg-Teller vibronic coupling phenomenologically through the expansion coefficient $\mu_{eg}^{(1)}$. As will be discussed in Sec. III, peak intensity in 2D EV and 2D VE spectra is proportional to the Franck-Condon factors and also sensitive to contributions from Herzberg-Teller vibronic couplings.

When a vibronic transition occurs in which the electronic state remains unchanged (i.e., $|g, v\rangle \rightarrow |g, n\rangle$ for $n = v \pm 1$ or $|e, v'\rangle \rightarrow |e, n'\rangle$ for $n' = v' \pm 1$), the electronic transition dipole moment goes to zero and the second term on the right-hand side of Eq. (8) vanishes, reducing $\mu^{a,b}$ to the vibrational transition moment. We let $\mathbf{M}_{vib}(Q) \equiv \mathbf{M}_{vn}(Q)$ to specify the vibrational transition $|g, v\rangle \rightarrow |g, n\rangle$ and $\mathbf{M}_{vib}(Q) \equiv \mathbf{M}_{v'n'}(Q)$ to denote $|e, v'\rangle \rightarrow |e, n'\rangle$. The nonlinear dependence of the vibrational transition moment is included through the Taylor expansion to account for electrical anharmonicity experienced by the nuclei during vibration in the system. For example, the electrical anharmonicity of a vibration in $|g\rangle$ is given by

$$\mathbf{M}_{vn}(Q) = \mu_{vn}^{(0)} + \sum_j \mu_{vn}^{(1)}Q_j + \frac{1}{2}\sum_{j,k}\mu_{vn}^{(2)}Q_jQ_k + \cdots, \tag{10}$$

where $\mu_{vn}^{(0)} = \mathbf{M}_{vn}(Q_0)$, $\mu_{vn}^{(1)} = \left(\frac{\partial\mathbf{M}_{vn}}{\partial Q_j}\right)_{Q_0}$, and $\mu_{vn}^{(2)} = \left(\frac{\partial^2\mathbf{M}_{vn}}{\partial Q_j\partial Q_k}\right)_{Q_0}$. This treatment assumes $\mathbf{M}_{vn}(Q) = \mu_{vn}^{(0)} + \mu_{vn}^{(1)}Q$ where $\mu_{vn}^{(1)} \neq 0$ which gives the selection rule for linear IR spectroscopy, $\Delta v = \pm 1$. The terms $\mu_{vn}^{(m)} \neq 0$ for $m \geq 2$ in Eq. (10) are related to the electrical anharmonicity of the vibration in the ground electronic state. Similar considerations applied to $\mathbf{M}_{v'n'}(Q)$ describe the nonlinearity of the vibration in the excited electronic state.

This explicit treatment of the electronic and vibrational transition moments allows the nonlinearity of the respective dipole moments to provide specific insight into the molecular system. The nonlinearity of the electronic transition moment ($\mathbf{M}_{eg}$) is relevant during the dynamic rearrangement of the electronic charge distribution that occurs upon transitioning between electronic states. In comparison, the nonlinearity of the vibrational transition moment ($\mathbf{M}_{vn}$ and $\mathbf{M}_{v'n'}$)

represents the nonlinearity of the nuclear motion for an instantaneous and relatively smaller shift in the electronic charge distribution that characterizes a single electronic state, $|g\rangle$ or $|e\rangle$.

Since the transition moment in Eq. (8) is completely generalized, we can concisely express the specific dipole moments and operators for each of the relevant transitions in 2D EV and 2D VE spectroscopies

$$\left(\text{for } \psi^a \in |g\rangle, \psi^b \in |g\rangle\right) \quad \mathbf{M}(Q) \to \mathbf{M}_{vn}(Q), \quad \mu^{a,b} \to \mu^{v,n}, \tag{11}$$

$$\left(\text{for } \psi^a \in |e\rangle, \psi^b \in |e\rangle\right) \quad \mathbf{M}(Q) \to \mathbf{M}_{v'n'}(Q), \quad \mu^{a,b} \to \mu^{v',n'}, \tag{12}$$

$$\left(\text{for } \psi^a \in |g\rangle, \psi^b \in |e\rangle\right) \quad \mathbf{M}(Q) \to \mathbf{M}_{eg}(Q), \quad \mu^{a,b} \to \mu^{e,g}. \tag{13}$$

The notation (eg, vn, and $v'n'$) in Eqs. (11)–(13) that specifies the transition dipole operators and matrix elements which reduce from the generalized $\mathbf{M}$ will be followed throughout this discussion.

III. THIRD ORDER NONLINEAR 2D EV AND 2D VE SPECTROSCOPIES

Much of the established formalism for other third order nonlinear techniques (e.g., 2D IR and 2D ES) can be applied to 2D EV and 2D VE spectroscopies.[46–50] Both 2D EV spectroscopy and 2D VE spectroscopy utilize sequential interactions [Figs. 1(a) and 1(b)] of three pulsed electric fields to generate the third order nonlinear polarization, $\mathbf{P}^{(3)}$, and measure the resultant electric field.[16–20,51] In the 2D EV experiment, the first two pulses, $\mathbf{E}_1$ and $\mathbf{E}_2$, are resonant with electronic transitions and the third interaction pulse, $\mathbf{E}_3$, is resonant with vibrational transitions in the ensemble. The ordering of the resonant field-matter interaction is reversed in the 2D VE experiment, where $\mathbf{E}_1$ and $\mathbf{E}_2$ resonantly excite vibrational transitions and $\mathbf{E}_3$ resonantly probes electronic transitions. In both of these 2D techniques, the correlations between electronic and nuclear motion are accessed directly by perturbing one degree of freedom with $\mathbf{E}_1$ and $\mathbf{E}_2$ while monitoring the response of the other degree of freedom with $\mathbf{E}_3$.

All of the microscopic molecular information is contained in the signal field that is emitted in the $\mathbf{k_{sig}}$ direction ($\mathbf{k_{sig}} = \pm\mathbf{k_1} \mp \mathbf{k_2} + \mathbf{k_3}$). The signal is generated by $\mathbf{P}^{(3)}$ which is a convolution of the third order material response function, $\overleftrightarrow{\mathbf{R}}^{(3)}$, and the three incident electric fields are shown as follows:

$$\begin{aligned}\mathbf{P}^{(3)}(\mathbf{k}_{sig}, t, \tau_2, \tau_1) &= \int_0^\infty \int_0^\infty \int_0^\infty \overleftrightarrow{\mathbf{R}}^{(3)}(\tau_3', \tau_2', \tau_1') \vdots \mathbf{E}_3(\mathbf{k}_3, t - \tau_3') \\ &\times \mathbf{E}_2(\mathbf{k}_2, t + \tau_2 - \tau_3' - \tau_2') \\ &\times \mathbf{E}_1(\mathbf{k}_1, t + \tau_2 + \tau_1 - \tau_3' - \tau_2' - \tau_1') d\tau_1' d\tau_2' d\tau_3'.\end{aligned} \tag{14}$$

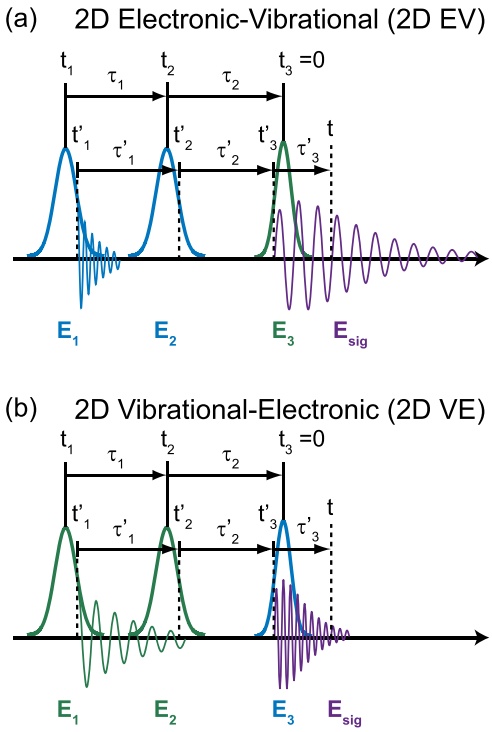

FIG. 1. 2D EV and 2D VE spectroscopy pulse sequences. Three input pulses (E_1, E_2, and E_3; blue or green) are controllably delayed to sequentially interact with a sample and generate the third order nonlinear polarization containing the 2D signal (E_{sig}, purple). The experimental delay times, τ_n, relate the time delay between pulse envelope maxima, t_n. The delays between successive field-matter interactions are specified by $\tau'_n = t'_{n+1} - t'_n$. (a) 2D electronic-vibrational: E_1 and E_2 are electronically resonant (blue) excitation interactions and E_3 is a vibrationally resonant (green) probe interaction. (b) 2D vibrational-electronic: E_1 and E_2 are vibrationally resonant (green) excitation interactions and E_3 is an electronically resonant (blue) probe interaction. Coherence is induced by E_1 at time t_1 that exists for a coherence period τ_1, and at time t_2, the field E_2 interacts with the system and collapses the coherence into population states that relax during the population time τ_2, then E_3 probes the molecular response to the initial perturbation at t_3.

The nonlinear response function $\overleftrightarrow{\mathbf{R}}^{(3)}$ contains the vibronic signal of interest and is expressed as a four-point correlation function of dipole moment operators with numbered subscripts (1-4) denoting the time-ordering of the field-matter interaction,

$$\begin{aligned}\overleftrightarrow{\mathbf{R}}^{(3)}(\tau_3', \tau_2', \tau_1') = \left(\frac{i}{\hbar}\right)^3 \Big\langle \Big[\Big[\Big[\mathbf{M}_4(\tau_3' + \tau_2' + \tau_1'), \\ \times \mathbf{M}_3(\tau_2' + \tau_1')\Big], \mathbf{M}_2(\tau_1')\Big], \mathbf{M}_1(0)\Big] \rho_0 \Big\rangle.\end{aligned} \tag{15}$$

Here, ρ_0 is the equilibrium reduced density matrix for the vibronic system eigenstates with its time evolution monitored during three separate time intervals (τ_1', τ_2', and τ_3' as described in Fig. 1) and the angled brackets $\langle \cdots \rangle$ denote the trace over the system and the bath degrees of freedom. Expanding the commutator in Eq. (15) yields eight terms grouped into four pairs of complex conjugate field-matter interaction pathways (see Sec. SI.1 of the supplementary material). $\overleftrightarrow{\mathbf{R}}^{(3)}$ is a fourth-rank tensor that contains the nonlinear vibronic response $R^{abcd}(\tau_3', \tau_2', \tau_1')$ and the orientational response $Y^{abcd}_{IJKL}(\tau_3', \tau_2', \tau_1')$ of the dipoles that interact with the various electric fields in all four conjugate

interaction pathways in the system,

$$\overleftrightarrow{\mathbf{R}}^{(3)}(\tau_3', \tau_2', \tau_1') = \sum_{\alpha=1}^{4} \sum_{IJKL} \sum_{a,b,c,d} (Y_\alpha)_{IJKL}^{abcd}(\tau_3', \tau_2', \tau_1') \times R_\alpha^{abcd}(\tau_3', \tau_2', \tau_1'). \quad (16)$$

In the above expression, the vibronic eigenstates are given by indices (a, b, c, d), where the indices $(IJKL)$ reference a permutation of the electric field polarization over the laboratory coordinates $\{X, Y, Z\}$. This paper solely focuses on the molecular insight contained in the nonlinear vibronic response function, $R^{abcd}(\tau_3', \tau_2', \tau_1')$, for various transition pathways where the indices (a, b, c, d) specify vibronic eigenstates interacting via $\mathbf{M}_{vn}$ [Eq. (11)], $\mathbf{M}_{v'n'}$ [Eq. (12)], and $\mathbf{M}_{eg}$ [Eq. (13)]. The response functions for all 2D EV and 2D VE peaks are listed in Sec. SI.2 of the supplementary material, and they are characterized by the combination of involved vibronic eigenstates in Tables SI.2.1 and SI.2.2 of the supplementary material.

We consider the system composed of two electronic states and one IR-active local vibrational mode, as described by $H_{vibronic}$ in Sec. II and depicted in Fig. 2. The parameters in the vibronic Hamiltonian are chosen so that the frequency of the anharmonic vibration is red-shifted in the excited electronic state. Using the transition frequencies shown in Fig. 2, the vibrational frequency difference between electronic states (Δ_{eg}) and the mechanical anharmonicity of the excited electronic state $(\Delta_{2',1'})$ can be defined as $\Delta_{eg} = \omega_{e,1'} - \omega_{g,1}$ and $\Delta_{2',1'} = \omega_{e,1'} - \omega_{e,2'}$. These expressions can be evaluated using stationary perturbation theory with second order energy corrections and are given in Sec. SI.3 of the supplementary material. For simplicity, it is assumed in Secs. III and IV that the electronically resonant electric fields have center frequency ω_{eg} and bandwidth $2\omega_{g,1}$, allowing resonant transitions between states with energy separation corresponding to frequencies within $\omega_{eg} \pm \omega_{g,1}$. The vibrationally resonant fields are assumed to have a sufficient bandwidth to excite

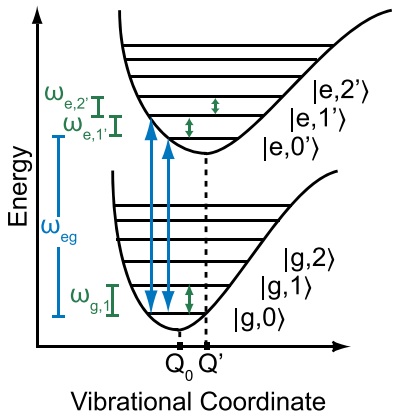

FIG. 2. An illustration (not drawn to scale) of the anharmonic potential energy surfaces represented by H_{vibronic} with linear and quadratic vibronic coupling. The states $|g,v\rangle$ and $|e,v'\rangle$ are the vibronic states in either the electronic ground, g, or excited, e, manifold with vibrational state v or v′, respectively. This model reflects a system of displaced, frequency shifted, anharmonic oscillators. The blue (green) arrows indicate transitions between electronic (vibrational) states. The frequencies ω_{eg}, $\omega_{g,v}$, and $\omega_{e,v'}$ correspond to the energy separation between the electronic manifolds, the vibrational levels in $|g\rangle$, and the vibrational levels in $|e\rangle$, respectively.

one-quantum transitions only. As the input electric fields have a finite pulse duration, it is important to distinguish between the experimentally controlled delay time (τ_n) and the delay between field-matter interactions (τ_n'). Section VI explores the effects of varying these electric field characteristics on the vibronic transition pathways accessible to the molecular system. Additionally, we assume the lowest vibrational transition energy in $|g\rangle$ to be larger than k_BT such that only $|g, 0\rangle$ is initially populated in the system and all transition pathways originate from this state. Next, we discuss the various rephasing and non-rephasing pathways contributing to the 2D EV and 2D VE signals and their manifestations in the peak positions, amplitudes, and line shapes of the resultant 2D spectra.

A. Vibronic signal pathways in 2D EV spectroscopy

Using the material and interaction Hamiltonians described in Sec. II and Fig. 2 and the center frequency and bandwidth considerations of the input electric fields described above, we can obtain the expression for the material response function and the third-order nonlinear polarization. The 2D EV response tensor, $\overleftrightarrow{\mathbf{R}}^{(3)}$, is obtained from Eq. (15) when $\mathbf{M}_1$ and $\mathbf{M}_2$ are electronic transition dipole moments and $\mathbf{M}_3$ and $\mathbf{M}_4$ are vibrational transition dipole moments. $\overleftrightarrow{\mathbf{R}}^{(3)}(\tau_3', \tau_2', \tau_1')$ includes responses from many possible vibronic transition pathways that the system can access during time intervals τ_n'. The possible vibronic Liouville pathways that can generate a 2D EV signal in the simplified system here while $\tau_2' \geq \tau_p$ are represented in the double-sided Feynman diagrams for the rephasing (R), $\mathbf{k_{sig}} = -\mathbf{k_1} + \mathbf{k_2} + \mathbf{k_3}$, and non-rephasing (NR), $\mathbf{k_{sig}} = +\mathbf{k_1} - \mathbf{k_2} + \mathbf{k_3}$, phase-matched directions [Figs. 3(a) and 3(b)]. The signals from the R and NR pathways oscillate at conjugate frequencies during the coherence period. Within the center frequency and bandwidth considerations described above, the system can only evolve in a population state of the density matrix during τ_2' when $\tau_2' \geq \tau_p$ and τ_p is the longer FWHM pulse duration between the optical and IR electric fields. Signals arising from off-diagonal density matrix elements during τ_2' when $\tau_2' \geq \tau_p$ are phase matched if the IR probe field bandwidth spans the vibrational frequencies of the fundamental (ω_{vib}) and first overtone $(2\omega_{vib})$ transitions. When $|\tau_2'| < \tau_p$, the time-ordering of the $\mathbf{k_2}$ and $\mathbf{k_3}$ field-matter interactions cannot be rigidly defined, and so the additional transition pathways in Fig. 3(c) can contribute to the 2D EV spectrum. These pathways will not yield new peaks, but they can contribute intensity to peaks I and III that oscillate at the τ_2' coherence frequency until the third field-matter interaction occurs. A fully absorptive cartoon spectrum for the system with linear and quadratic vibronic coupling is illustrated in Fig. 3(d). The mth peak consists of signal contributions from the corresponding R $(D_{R,m}^{EV})$ and NR $(D_{NR,m}^{EV})$ double-sided Feynman diagrams. The complete set of vibronic response functions for each of the diagrams is given in the supplementary material. In general, the response function consists of (i) oscillating frequencies which determine the position of the 2D peak in the ω_1 and ω_3 Fourier space, (ii) the product of transition dipole factors which govern the amplitude of the 2D peaks, and (iii) a nonlinear

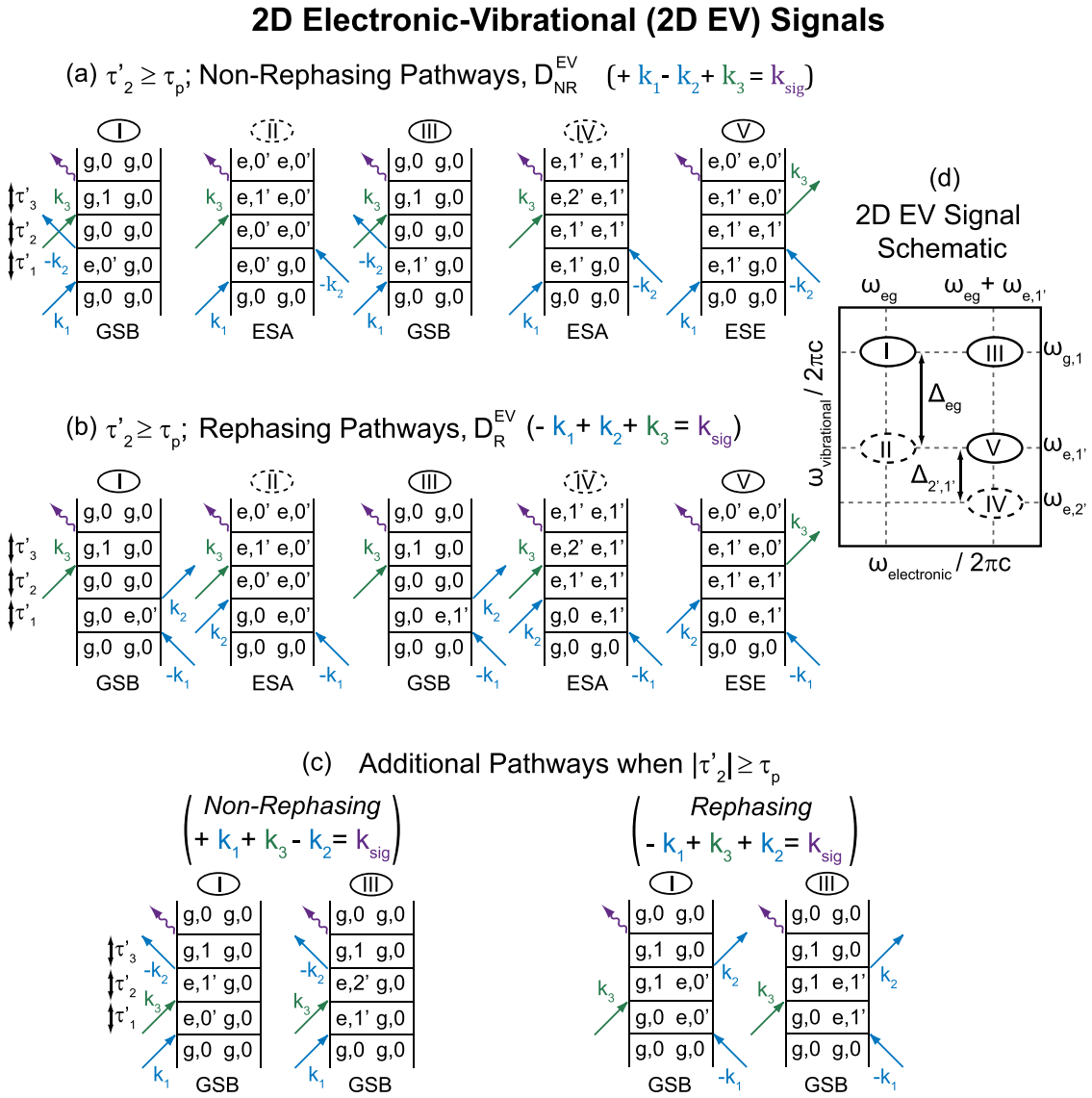

FIG. 3. 2D EV vibronic signals overview. All the accessible Liouville transition pathways [(a)–(c)] are given for the case that the excitation fields ($\mathbf{k_1}$ and $\mathbf{k_2}$) span frequencies $\omega_{eg} \pm \omega_{g,1}$ [where $\omega_{eg} = (E_{e,0'} - E_{g,0})/\hbar$ and $\omega_{g,v} = (E_{g,(v+1)} - E_{g,v})/\hbar$], and the probe field ($\mathbf{k_3}$) has a bandwidth sufficient to resonantly excite single quantum vibrational transitions only. The 2D EV non-rephasing (NR) and rephasing (R) signal pathways represented by the double-sided Feynman diagrams D_{NR}^{EV} and D_R^{EV} in (a) and (b), respectively, represent the contributing 2D EV signal pathways when $\mathbf{k_2}$ and $\mathbf{k_3}$ are beyond temporal overlap (i.e., $\tau_2' \geq \tau_p$ where τ_p is the longer pulse FWHM duration) such that field-matter interaction time ordering is unambiguous. Additional pathways in (c) contribute only during the $\mathbf{k_2}$ and $\mathbf{k_3}$ temporal overlap ($|\tau_2'| < \tau_p$). The diagrams have peak labels (I-V) denoting the signal to which that pathway contributes; the R and NR diagrams for a given peak sum to yield the absorptive 2D EV signal. The diagrams are also specified by transition type: ground state bleach (GSB, positive, solid line), excited state absorption (ESA, negative, dashed line), and excited state stimulated emission (ESE, positive, solid line). The illustrated absorptive 2D EV spectrum shown (d) for a system where $V_j^{(1)} \neq 0$ and $V_{j,j}^{(2)} \neq 0$ gives peaks I-V at the coordinates $\omega_1 = \omega_{eg}$, $\omega_{eg} + \omega_{e,1'}$ and $\omega_3 = \omega_{g,1}$, $\omega_{e,1'}$, and $\omega_{e,2'}$ [where $\omega_{e,v'} = (E_{e,(v+1)'} - E_{e,v'})/\hbar$]; thus, the frequency difference of the vibration in $|g\rangle$ and $|e\rangle$, $\Delta_{eg} = \omega_{e,1'} - \omega_{g,1}$, and the anharmonicity in $|e\rangle$, $\Delta_{2'1'} = \omega_{e,1'} - \omega_{e,2'}$, can be read off the 2D EV spectrum directly.

dephasing function $[F^{a,b,c,d}(\tau_3', \tau_2', \tau_1')]$ that dictates the 2D line shape. Each of these factors is discussed in detail below.

1. 2D EV peak positions

The 2D EV peak positions identify specific vibrational modes coupled to electronic transitions in the molecular system, and they reveal differences between the ground and excited potential energy surfaces. These positions are dictated by the energy separation of the vibronic eigenstates in the molecular ensemble. In the vibronic systems modeled by $H_{vibronic}$, the eigenstate energies are dependent on the vibrational anharmonicity, the equilibrium position displacement in the excited state, and the excited state frequency shift. The peak positions in the $\omega_{electronic}$ dimension indicate the resonance frequencies of the electronic transition $|g, 0\rangle \rightarrow |e, v'\rangle$ that are accessed during the electronic coherence time, τ_1'. The positions in the $\omega_{vibrational}$ dimension reveal vibrational modes that are coupled to the electronic transitions. As opposed to degenerate 2D techniques where peaks can exist in the absence of molecular coupling (i.e., on-diagonal peaks), every peak in 2D EV spectroscopy is a cross peak and requires the coupling of electronic and vibrational degrees of freedom to be observed.

Peaks I and II [Fig. 3(d)] are centered at $\omega_{electronic} = \omega_{eg}$ because the Liouville pathways that contribute to these signals evolve in the coherence between $|g,0\rangle$ and $|e,0'\rangle$ during τ_1'. The Liouville pathways that give rise to peaks I and II differ by the vibronic state population $|g,0\rangle\langle g,0|$ or $|e,0'\rangle\langle e,0'|$ in which the system evolves, respectively, during τ_2'. Therefore, the final probe field interaction is resonant with either $\omega_{g,1}$ or $\omega_{e,1'}$ to yield a ground state bleach [peak I, $(\omega_{eg},\omega_{g,1})$] or an excited state absorption [peak II, $\left(\omega_{eg},\omega_{e,1'}\right)$] signal, respectively. Peaks III-V have peak centers $\omega_{electronic} = \omega_{eg} + \omega_{e,1'}$ that reflect vibronic transition pathways with electronic coherence between $|g,0\rangle$ and $|e,1'\rangle$ during τ_1', the vibrationally probed transitions originate from τ_2' populated states of either $|g,0\rangle\langle g,0|$ or $|e,1'\rangle\langle e,1'|$. When higher lying vibrational states ($v' > 0$) in $|e\rangle$ are accessed, the excited state stimulated emission (ESE) Liouville pathway ($D_{R,V}^{EV}$, $D_{NR,V}^{EV}$) is possible. Hence, three 2D EV peaks exist for each pathway with electronic coherence between $|g,0\rangle$ and $|e,(v' > 0)\rangle$ in τ_1'. In the case where both linear and quadratic vibronic couplings are present, peaks III (GSB), IV (ESA), and V (ESE) may be observed at $\left(\omega_{eg} + \omega_{e,1'}, \omega_{g,1}\right)$, $\left(\omega_{eg} + \omega_{e,1'}, \omega_{e,2'}\right)$, and $\left(\omega_{eg} + \omega_{e,1'}, \omega_{e,1'}\right)$, respectively.

In 2D EV spectroscopy, the ESE is the only transition pathway that can yield positive signals from a vibrational transition in the electronic excited state, which provides an important contrast to the negative ESA signals arising from populated vibronic states in $|e\rangle$. The other source of positive signals is the GSB pathway, which will only result from vibrational transitions in $|g\rangle$. Therefore, the GSB and ESE signals are specific to vibrations in the ground and excited electronic states, respectively. As we will see later, the intensity contributions from these positive signals will be separable in the ω_3 dimension when the anharmonic vibration is frequency-shifted in the excited state. A systematic discussion of how the anharmonicity, excited state equilibrium displacement, and excited state frequency shifting affect the presence of 2D EV peaks is accompanied by simulated 2D EV spectra in Sec. IV.

2. 2D EV peak amplitudes

The 2D EV peak amplitudes are determined by the population of molecules in $|g,0\rangle$ and the relative strength of the four interacting dipoles that generate the third order response, as shown in Eqs. (SI.2.4) and (SI.2.5) of the supplementary material. Generally, the effects of electrical anharmonicity in the system arise from the nonlinearity of the dipole moments with respect to the vibrational coordinate and have been considered in 2D IR spectroscopy. The explicit treatment of both the electronic and vibrational dipole moments in 2D EV and 2D VE spectroscopies can provide insight into the electrical anharmonicity of the molecule from two perspectives: (1) the nuclear dependence of the electronic redistribution upon changing electronic states and (2) the nonlinearity of a vibration in an excited electronic state.

The dependence of $\mathbf{M}_{eg}(Q)$ on the vibrational coordinates appears when the coefficients $\mu_{eg}^{(1)}$ and $\mu_{eg}^{(2)}$ are nonzero in the expression for $\mu^{e,g}$ given by

$$\mu^{e,g} = \mu_{eg}^{(0)}\langle g,v|\,e,v'\rangle + \mu_{eg}^{(1)}\sum_j \langle g,v|\,Q_j\,|e,v'\rangle + \frac{1}{2}\mu_{eg}^{(2)}\sum_j \langle g,v|\,Q_jQ_j\,|e,v'\rangle + \cdots, \tag{17}$$

which is obtained by evaluating Eq. (8) for a vibronic transition [i.e., subject to Eq. (13)]. The Condon approximation requires that the electronic transition is independent of the nuclear coordinates, implying $\mu_{eg}^{(m)} = 0$ for $m \geq 1$. In this case, $\mu^{e,g}$ expresses the electronic transition dipole moment for the system at the equilibrium nuclear configuration with the transition strength modulated by the overlap integral of the two involved vibronic states. The zeroth order result implies the reduction of the Born-Oppenheimer adiabatic wave functions to crude adiabatic wave functions because of the constraints imposed by referencing only the equilibrium nuclear configuration;[39,43,44] these constraints are corrected when higher order terms are included. Therefore, to zeroth order, the amplitudes of the 2D EV peaks are directly proportional to $|\mu^{e,g}|^2 = \left|\mu_{eg}^{(0)}\right|^2|\langle g,v\,|\,e,v'\rangle|^2$ due to the first two interactions of $\mathbf{M}_{eg}(Q)$ with the density matrix in the nonlinear vibronic response function [Eq. (15)]. This directly demonstrates that all 2D EV peak amplitudes are scaled by the Franck-Condon factors, $|\langle g,v\,|\,e,v'\rangle|^2$.

For electronic transitions that are dependent on nuclear coordinates, the linear and higher order terms in Eq. (9) may be nonzero, and they account for variations in the vibronic transition strength due to the nuclear configuration of the system. This is known as the breakdown of the Condon approximation.[41–43] If the Condon approximation is relaxed, then the higher order terms that collectively describe the non-Condon effects ($\mu_{eg}^{(m)} \neq 0$ for $m \geq 1$) are included in evaluating $\mu^{e,g}$, and the vibronic transition strength deviates from the zeroth order scaling with the Franck-Condon factor. This demonstrates that the 2D EV peak amplitudes are sensitive to non-Condon effects through intensity contributions from the first and higher order terms in $\mu^{e,g}$. The amplitude ratio that compares 2D EV peaks originating from the vibronic transitions $|g,v\rangle \rightarrow |e,v'\rangle$ and $|g,v\rangle \rightarrow |e,(v+1)'\rangle$ [e.g., peaks I and III in Fig. 3(d)] should be equal to the ratio of the respective Franck-Condon factors if non-Condon effects are negligible; variations from this amplitude ratio reflect the presence of non-Condon effects.

Effects from the system electrical anharmonicity in the vibration can also be present from the nonlinearity of the vibrational transition dipole moment, in a similar fashion to 2D IR spectroscopy.[47,48,52] The influence of this type of electrical anharmonicity in 2D EV spectroscopy is observed specifically for the vibration in the electronic excited state. A linear dependence of $\mu^{v',n'}$ on the nuclear coordinates yields transition dipoles for the $|e,0'\rangle \rightarrow |e,1'\rangle$, $\left(\mu^{0',1'}\right)$, and for the $|e,1'\rangle \rightarrow |e,2'\rangle$, $\left(\mu^{1',2'}\right)$, transitions that should scale harmonically as $\mu^{1',2'} = \sqrt{2}\mu^{0',1'}$. Comparison of oppositely signed peak amplitudes for an electronically excited state vibration [e.g., peaks IV and V in Fig. 3(d)] will reflect the electrical

anharmonicity of the vibrational mode in the excited electronic state specifically.

3. 2D EV line shapes

The influence of the system-bath dynamics are reflected in the 2D EV line shapes which are described by the nonlinear dephasing function for each vibronic signal pathway. Following the approach of Sung and Silbey,[37] the dephasing functions, $F^{a,b,c,d}(\tau_3', \tau_2', \tau_1')$, in the nonlinear vibronic response are composed of line shape functions, $h_{a,b}(t)$ (defined in Sec. SI.1 of the supplementary material), that describe the time-dependent transition frequency fluctuation between vibronic states $|a\rangle$ and $|b\rangle$ induced by system-bath dynamics. Assuming that the transition frequency fluctuations $[\delta\omega_{a,b}(t)]$ about an ensemble average frequency $(\bar{\omega}_{a,b})$ obey Gaussian statistics, the time dependence of a resonant transition frequency is expressed as $\omega_{a,b}(t) = \bar{\omega}_{a,b} + \delta\omega_{a,b}(t)$. The energy gap correlation function $\zeta_{a,b}$ correlates the transition frequency fluctuation $\delta\omega_{a,i}$ with the fluctuation $\delta\omega_{b,i}$ over a time period t where the subscript "i" is the initial state of the density matrix. The time scales for these fluctuations are expressed as auto-correlation and cross correlation, which describe the correlation of a single vibronic transition (a = b) or of two different vibronic transitions (a ≠ b), respectively. The energy gap correlation function can be expressed in terms of these transition frequency fluctuations by $\zeta_{a,b}(t) = \langle \delta\omega_{a,i}(t)\delta\omega_{b,i}(0)\rangle$.

We use a simplified notation to express the correlation functions in 2D EV and 2D VE spectroscopies. Instead of specifying the correlated eigenstates, the subscripts specify the transition frequency between the correlated eigenstates (i.e., $eg = |g,0\rangle \rightarrow |e,0'\rangle$, $v = |g,0\rangle \rightarrow |g,1\rangle$, and $v' = |e,0'\rangle \rightarrow |e,1'\rangle$). The energy gap auto-correlation functions are the fluctuations in the electronic transition frequency ($\zeta_{eg,eg}$), the ground state vibrational frequency ($\zeta_{v,v}$), and the excited state vibrational frequency ($\zeta_{v',v'}$). The cross correlation functions ($\zeta_{eg,v}$, $\zeta_{eg,v'}$, $\zeta_{v,v'}$) relate the frequency fluctuations in electronic transitions and vibrational transitions. The correlation functions are defined in Appendix A. Both 2D EV and 2D VE spectroscopies access all of the auto-correlation functions. The 2D EV experiment only accesses the $\zeta_{eg,v'}$ cross correlation, while the 2D VE line shapes include contributions from all three cross correlations. However, as shown below, the line shapes in both techniques can be defined in terms of the same correlation functions and a proportionality constant.

Electronic-state-dependent vibrational dephasing is explored by defining a proportionality constant, λ, that relates the ratio of the excited electronic state fluctuations to those in the ground electronic state,

$$\lambda = \frac{\delta\omega_{e1',e0'}(t)}{\delta\omega_{g1,g0}(t)}. \tag{18}$$

This parameter is analogous to the α_0 and α_1 parameters used by Lewis *et al.*[23] Now the 2D line shapes can be written in terms of only three energy gap correlation functions ($\zeta_{eg,eg}$, $\zeta_{eg,v}$, and $\zeta_{v,v}$) and λ,

$$\zeta_{v',v'} = \lambda^2\zeta_{v,v}, \tag{19}$$

$$\zeta_{v,v'} = \lambda\zeta_{v,v}, \tag{20}$$

$$\zeta_{eg,v'} = \lambda\zeta_{eg,v}. \tag{21}$$

As shown below, expressing the dephasing functions in terms of auto-correlation and cross correlation functions demonstrates that 2D EV and 2D VE spectroscopies are sensitive to the coupling between electronic and vibrational degrees of freedom in a molecular ensemble. Additionally, obtaining a proportionality constant relating the nature of the homogeneous vibrational dephasing in the ground and the excited electronic manifolds is a notable advantage of these spectroscopies.

In this work, we assume the homogeneous limit where the fluctuations $\delta\omega_{y,i}(t)$ are much faster than the time scale of the experimental measurement and that fluctuations in the mechanical anharmonicity are negligible. In this limit, the line shape functions become linear with respect to time, $h_{a,b}(t) \approx \Gamma_{a,b}t$, and the dephasing functions ($F^{a,b,c,d}$) reduce to exponentially decaying functions where the $\Gamma_{a,b}$ terms are damping constants, or decay times, that reflect the homogenous dephasing time scales defined as $\Gamma_{a,b} = \int_0^\infty d\tau\zeta_{a,b}(\tau)$. The absorption line shapes are related by the Fourier transform of the dephasing functions, which yield 2D Lorentzian line shapes with spectral widths in ω_1 and ω_3 defined by the $\Gamma_{a,b}$ terms for the τ_1' and τ_3' periods, respectively. In future work, we will explore the effects of correlated spectral broadening in these 2D spectroscopies. The 2D EV dephasing functions, $F^{a,b,c,d}_{R,I-V}$, for all five peaks are expressed (R and NR functions have the same form, only R is given) using simplified notations

$$F^{g0,g1,g0,e0'}_{R,I}(\tau_3', \tau_2', \tau_1') = \Gamma_{v,v}\tau_3' + \Gamma_{eg,eg}\tau_1', \tag{22}$$

$$F^{g0,e0',e1',e0'}_{R,II}(\tau_3', \tau_2', \tau_1') = (\lambda^2)\Gamma_{v,v}\tau_3' + \Gamma_{eg,eg}\tau_1', \tag{23}$$

$$F^{g0,g1,g0,e1'}_{R,III}(\tau_3', \tau_2', \tau_1') = \Gamma_{v,v}\tau_3' + \left[\Gamma_{eg,eg} + (2\lambda)\Gamma_{eg,v} + (\lambda^2)\Gamma_{v,v}\right]\tau_1', \tag{24}$$

$$F^{g0,e1',e2',e1'}_{R,IV}(\tau_3', \tau_2', \tau_1') = (\lambda^2)\Gamma_{v,v}\tau_3' + \left[\Gamma_{eg,eg} + (2\lambda)\Gamma_{eg,v} + (\lambda^2)\Gamma_{v,v}\right]\tau_1', \tag{25}$$

$$F^{g0,e1',e0',e1'}_{R,V}(\tau_3', \tau_2', \tau_1') = (\lambda^2)\Gamma_{v,v}\tau_3' + \left[\Gamma_{eg,eg} + (2\lambda)\Gamma_{eg,v} + (\lambda^2)\Gamma_{v,v}\right]\tau_1'. \tag{26}$$

The sensitivity of 2D EV spectroscopy to electronic-state-dependent vibrational dephasing is demonstrated by the λ^2 dependence of peaks II, IV, and V during the detection period τ_3'. The comparison of these broadened peaks to peaks I and III in the $\omega_{vibrational}$ dimension will directly reveal electronic-state-dependent vibrational dephasing. There is also a strong, uniform λ dependence in the $\omega_{electronic}$ dimension for peaks

III, IV, and V, which may reflect deviations from strictly vertical electronic excitation and stronger fluctuations of "hot" vibrations in $|e\rangle$.

B. Vibronic signal pathways in 2D VE spectroscopy

Similar to Sec. III A, we will use the material and interaction Hamiltonians described in Sec. II and Fig. 2 and the center frequency and bandwidth considerations of the input electric fields described above to obtain the expression for the material response function and the third-order nonlinear polarization for the 2D VE experiment. In contrast to 2D EV experiments, no vibrational transitions in the excited electronic state are directly observed in 2D VE spectroscopy. Rather, the resonance frequencies of the electronic transitions that are probed with the final probe interaction carry this information. The only vibrationally resonant field-matter interaction in 2D VE spectroscopy occurs with the first two pulses with frequency $\omega_{g,1}$. The electronic transitions probed with $\mathbf{k}_3$ have energies equal to the sum of the electronic energy gap and some combination of vibrational quanta [see Fig. 4(d)]. As a result, the direct comparison of specific peaks that report on vibrational

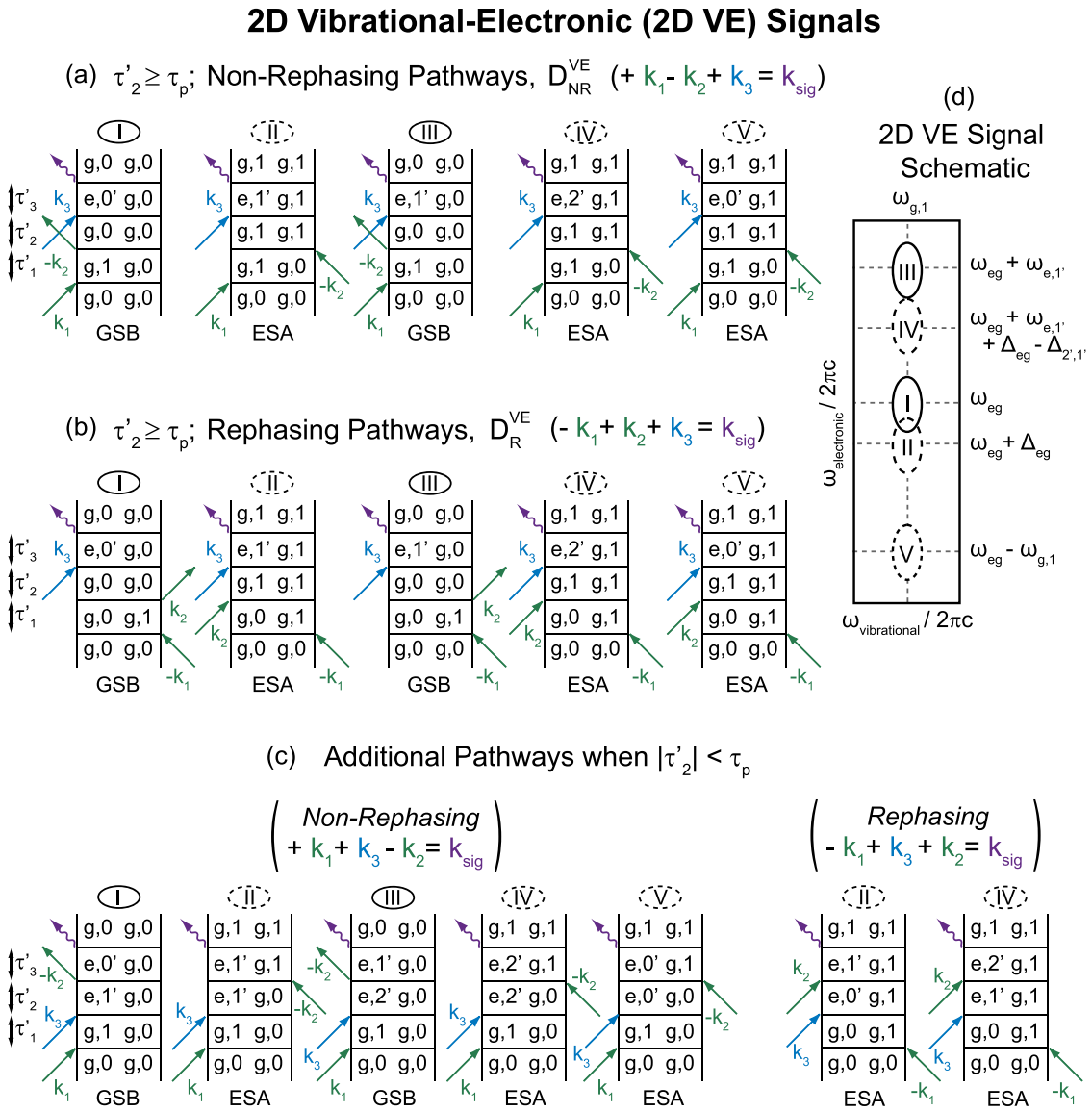

FIG. 4. 2D VE vibronic signals overview. The relevant Liouville pathways that contribute to the 2D VE signal when the excitation fields ($\mathbf{k}_1$ and $\mathbf{k}_2$) have a sufficient bandwidth for resonant single quantum vibrational transitions and the probe field ($\mathbf{k}_3$) spans frequencies $\omega_{eg} \pm \omega_{g,1}$. The non-rephasing (NR) and rephasing (R) signal pathways represented by the double-sided Feynman diagrams D_{NR}^{VE} and D_{R}^{VE} in (a) and (b), respectively, are the only contributing 2D VE signal pathways when $\mathbf{k}_2$ and $\mathbf{k}_3$ are beyond temporal overlap (i.e., $\tau_2' \geq \tau_p$ where τ_p is the longer pulse FWHM duration) such that the field-matter interaction time ordering is well defined. Additional pathways in (c) contribute only during the $\mathbf{k}_2$ and $\mathbf{k}_3$ temporal overlap ($|\tau_2'| < \tau_p$). The peak labels (I-V) specify the signal to which that pathway contributes; the R and NR diagrams for a given peak sum to yield the absorptive 2D VE signal. The diagrams are also categorized by signal type: ground state bleach (GSB, positive, solid line) and excited state absorption (ESA, negative, dashed line). The fully absorptive 2D VE spectrum is depicted (d) for a system where $V_j^{(1)} \neq 0$ and $V_{j,j}^{(2)} \neq 0$; peaks I-V share the excitation frequency coordinate $\omega_1 = \omega_{g,1}$ and they are distinguished by the probed electronic transition frequencies $\omega_3 = \omega_{eg}$, $\omega_{eg} + \Delta_{eg}$, $\omega_{eg} + \omega_{e,1'}$, $\omega_{eg} + \omega_{e,1'} + \Delta_{eg} - \Delta_{2'1'}$, and $\omega_{eg} - \omega_{g,1}$ where the frequencies are defined as $\omega_{eg} = (E_{e,0'} - E_{g,0})/\hbar$, $\omega_{g,v} = (E_{g,(v+1)} - E_{g,v})/\hbar$, $\omega_{e,v'} = (E_{e,(v+1)'} - E_{e,v'})/\hbar$, the frequency difference of the vibration in $|g\rangle$ and $|e\rangle$, $\Delta_{eg} = \omega_{e,1'} - \omega_{g,1}$, and the anharmonicity in $|e\rangle$, $\Delta_{2'1'} = \omega_{e,1'} - \omega_{e,2'}$.

features in the ground and excited electronic states is not as straightforward as in 2D EV. The reader is directed to recent papers by Courtney *et al.*[17,18] for additional discussion of 2D VE transitions.

Considering the same electric field parameters described earlier, the allowed transition pathways in 2D VE only evolve in population states during τ_2' while $\tau_2' \geq \tau_p$. The 2D VE response tensor is obtained from Eq. (15) when $\mathbf{M}_1$ and $\mathbf{M}_2$ are vibrational transition dipole moments and when $\mathbf{M}_3$ and $\mathbf{M}_4$ correspond to electronic transition dipole moments. The transition pathways available to a molecular system described by $H_{vibronic}$ for the vibronic system in the present discussion are shown as double-sided Feynman diagrams in Figs. 4(a) and 4(b), and a fully absorptive 2D VE spectrum is illustrated in Fig. 4(d). The complete set of vibronic response functions for each of the diagrams in Fig. 4 is given in the supplementary material. In general, the 2D VE response function consists of (i) oscillating frequencies that determine the position of the 2D peak in the ω_1 and ω_3 Fourier space, (ii) product of transition dipole factors that govern the amplitude of the 2D peaks, and (iii) nonlinear dephasing function $[F^{a,b,c,d}(\tau_3', \tau_2', \tau_1')]$ that dictates the 2D line shape. We will discuss each of these factors in detail below.

1. 2D VE peak positions

The 2D VE peak positions encode the modulation of the electronic energy gap that is coupled to the nuclear motion of the ground electronic state molecule. The resonance frequencies for the transitions between the vibronic eigenstates modeled by $H_{vibronic}$ govern the positions of the 2D VE peaks. Thus, the 2D VE peak positions are sensitive to the anharmonicity, the excited state equilibrium displacement, and the excited state frequency shift of the vibrational mode. The $\omega_{vibrational}$ peak position indicates the resonant vibrational transition that is initially excited in the ground state molecule during τ_1', and the peak coordinate along the $\omega_{electronic}$ dimension reflects the energy gap for transitioning into a vibrational state in $|e\rangle$ following the initial vibrational perturbation. Given the considered electric field characteristics, 2D VE transition pathways are resonantly excited with the same excitation frequency $\omega_{g,1}$ resulting in the vertically stacked series of peaks shown in Fig. 4(d). Resolution of different peaks in the $\omega_{vibrational}$ dimension becomes relevant when more than one vibrational mode is involved in the vibronically coupled system, which could include other high frequency vibrational modes or low frequency structural modes. Since the 2D VE transition pathways never include a vibrationally resonant field-matter interaction with a vibration in $|e\rangle$, there will not be the same peak separation along $\omega_{vibrational}$ that reflects Δ_{eg} and $\Delta_{2'1'}$ as occurs in 2D EV spectra. Instead, the peak separation in the $\omega_{electronic}$ dimension is due to the modulation of the electronic energy gap by Δ_{eg} and $\Delta_{2'1'}$ which are expressed as combinations of vibrational quanta.

A particularly notable feature of 2D VE spectroscopy is the absence of ESE pathways to contribute positive intensity to the spectrum. In general, observed peaks will be broad in the ω_3 dimension due to the electronic transitions that are probed with this technique. The ability to resolve information about the excited electronic state potential energy surface depends on the nature and strength of the system's vibronic coupling and the extent of overlap between these inherently broad signals. Peaks I-IV consist of pairs of bleach and absorption features that have frequency separation on the order of a fraction of one vibrational quantum (i.e., Δ_{eg} and $\Delta_{2'1'}$). The comparison of the peak separation and the electronic absorption line width dictates the overlap of oppositely signed 2D VE signals.

The sign of the peaks in the 2D VE spectrum differ by the populated state over which the system evolves during τ_2'. The positive GSB features arise from electronic transitions into $|e\rangle$ from $|g,0\rangle\langle g,0|$, and the negative ESA features result from electronic transitions originating from $|g,1\rangle\langle g,1|$. Peak I (GSB) is centered at $\omega_{electronic} = \omega_{eg}$ because $\mathbf{k_3}$ induces the transition $|g,0\rangle \rightarrow |e,0'\rangle$, while peak II (ESA) is separated from peak I in $\omega_{electronic}$ by Δ_{eg} since the $\mathbf{k_3}$ interactions yielding peak II induce the transition $|g,1\rangle \rightarrow |e,1'\rangle$. For the red-shifted anharmonic vibration in $|e\rangle$ discussed here, $\omega_{e,1'} < \omega_{g,1}$ and so Δ_{eg} is negative resulting in the separation of peaks I and II represented in Fig. 4(d); if $\omega_{e,1'} = \omega_{g,1}$, then $\Delta_{eg} = 0$ and peaks I and II are centered at the same 2D VE spectral coordinates ($\omega_{g,1}$,ω_{eg}). Therefore, the difference between the ground and excited electronic state vibrations is contained in the peak separation of peaks I and II, similar to 2D EV. Generally, peaks III (GSB) and IV (ESA) include electronically resonant field-matter interactions higher in energy by $\sim \hbar\omega_{e,1'}$ than those that contribute to peaks I and II. The probed electronic transitions in peaks III and IV are $|g,0\rangle \rightarrow |e,1'\rangle$ and $|g,1\rangle \rightarrow |e,2'\rangle$, respectively. Peak IV is lower in frequency than peak III in $\omega_{electronic}$ by Δ_{eg} and the excited state mechanical anharmonicity, $\Delta_{2'1'}$. As a result, the 2D VE spectrum of a red-shifted anharmonic vibrational mode will have greater $\omega_{electronic}$ separation between peaks III and IV than between peaks I and II. Thus, when vibronic states $|e,v'\rangle$ for $v' > 1$ are resonantly accessed via $\mathbf{k_3}$, information about $\Delta_{2'1'}$ is included in the 2D VE spectral features. Peak V (ESA) is not paired with an oppositely signed and overlapping peak. The electronically resonant probe transition that generates peak V utilizes the lower frequency portion of the available bandwidth in $\mathbf{k_3}$ for the transition $|g,1\rangle \rightarrow |e,0'\rangle$; therefore, no lower-lying vibrational state in $|e\rangle$ exists to provide the accompanying positive GSB peak that is observed for peaks I-IV. Peak V is a unique spectral signature in 2D VE as it is inherently less convoluted by other spectral signatures.

2. 2D VE peak amplitudes

The 2D VE peak amplitudes depend on the initial ground state population and the strength of the four interacting dipoles of the vibronic system, as shown by the 2D VE response function [see Eqs. (SI.2.6) and (SI.2.7) of the supplementary material]. The nonlinear nuclear coordinate dependence of the electronic transition dipole as given by Eq. (17) and the vibrational transition dipoles inherently contribute to the resonant vibronic transitions in 2D VE spectroscopy. However, the effects of the nonlinearity of $\mathbf{M}_{eg}(Q)$ will overwhelm any effects of electrical anharmonicity in $\mathbf{M}_{vn}(Q)$ and $\mathbf{M}_{v'n'}(Q)$

present in 2D VE spectra. The direct observation of the electrical anharmonicity of a vibration in a particular electronic state requires the comparison of features arising from vibrational transitions between a zero and one quantum state and between a one and two quantum state (e.g., $\mu^{0',1'}$ and $\mu^{1'2'}$). Since 2D VE transition pathways include only one vibrationally resonant field-matter interaction, no such comparison is easily extracted from the spectra.

An important advantage of 2D VE spectroscopy is that the experiment samples a larger variety of transitions between vibronic states in different electronic manifolds as the electronically resonant field-matter interaction is the probe interaction. The pathways that contribute the negative ESA features evolve in $|g,1\rangle\langle g,1|$ during τ_2', which allows the electronic transition to originate from an excited vibrational state in $|g\rangle$ and access higher vibrational states in $|e\rangle$ than is possible in the GSB pathways. This means that an amplitude comparison between GSB and ESA peak pairs includes the magnitudes of the involved dipole moments and the magnitudes of two different vibronic overlap integrals. For example, to the zeroth order in $\mathbf{M}_{eg}(Q)$ [Eq. (9)], the amplitude comparison of peaks I and II considers the difference in magnitudes of Franck-Condon factors for the $|g,0\rangle \rightarrow |e,0'\rangle$ and $|g,1\rangle \rightarrow |e,1'\rangle$ transitions. Similar to 2D EV spectroscopy, the non-Condon effects will manifest themselves as amplitude changes in the 2D VE spectra and will be explored in detail in Sec. IV.

3. 2D VE line shapes

The nonlinear dephasing functions determine the line shapes observed in 2D VE spectra. As described for 2D EV line shapes in the homogenous limit above, the formulation of the 2D VE dephasing functions in terms of autocorrelation and cross correlation functions demonstrates that 2D VE spectroscopy is sensitive to fluctuations of vibronic frequencies. While the 2D VE dephasing functions are defined by more cross correlations, the simplification of these expressions using the λ parameter [Eq. (18)] shows that 2D EV and 2D VE can be described by the same three correlation functions. However, the dephasing functions for 2D VE are very different from those in 2D EV, which is a result of the different sequences of field-matter interactions utilized, and they are expressed for the rephasing contributions to the five peaks as follows:

$$F_{R,I}^{g0,e0',g0,g1}(\tau_3',\tau_2',\tau_1') = \Gamma_{eg,eg}\tau_3' + \Gamma_{v,v}\tau_1', \tag{27}$$

$$F_{R,II}^{g0,g1,e1',g1}(\tau_3',\tau_2',\tau_1') = \left[\Gamma_{eg,eg} + 2(\lambda-1)\Gamma_{eg,v} + (\lambda-1)^2\Gamma_{v,v}\right]\tau_3' + \Gamma_{v,v}\tau_1', \tag{28}$$

$$F_{R,III}^{g0,e1',g0,g1}(\tau_3',\tau_2',\tau_1') = \left[\Gamma_{eg,eg} + 2(\lambda)\Gamma_{eg,v} + (\lambda)^2\Gamma_{v,v}\right]\tau_3' + \Gamma_{v,v}\tau_1', \tag{29}$$

$$F_{R,IV}^{g0,g1,e2',g1}(\tau_3',\tau_2',\tau_1') = \left[\Gamma_{eg,eg} + 2(2\lambda-1)\Gamma_{eg,v} + (2\lambda-1)^2\Gamma_{v,v}\right]\tau_3' + \Gamma_{v,v}\tau_1', \tag{30}$$

$$F_{R,V}^{g0,g1,e0',g1}(\tau_3',\tau_2',\tau_1') = \left[\Gamma_{eg,eg} - 2\Gamma_{eg,v} + \Gamma_{v,v}\right]\tau_3' + \Gamma_{v,v}\tau_1'. \tag{31}$$

The λ dependence is limited to only the ω_3 probe dimension in 2D VE spectra, given the excitation is vibrationally resonant. Peaks II, III, and IV have varying extents of quadratic λ dependence. Notably, while peak V is the uniquely isolated peak in 2D VE spectra, it carries no information reflecting electronic-state-dependent vibrational dephasing. Peak I is the only peak that does not contain contributions from the cross correlation, whereas in 2D EV, both GSB peaks (I and III) did not include cross correlation information. Finally, the nontrivial cancellation between oppositely signed spectral contributions in 2D VE may complicate spectra since GSB and ESA peak pairs (e.g., III and IV) will have different amplitude contributions due to electronic-state-dependent vibrational dephasing.

IV. 2D EV AND 2D VE SIMULATIONS

The 2D VE and 2D EV spectra are simulated in this section by calculating the response functions for all the contributing vibronic transition pathways when the electronically resonant transitions occur within the frequency range $\omega_{electronic} = \omega_{eg} \pm \omega_{g,1}$ and the vibrationally resonant transitions occur for single quantum transitions (Δv, $\Delta v' = \pm 1$) only. We further assume that all the electric fields are much shorter in time than the dynamics of interest, that $\tau_2' > 0$ such that only the diagrams in Figs. 3(a), 3(b), 4(a), and 4(b) are relevant, and that τ_2' is sufficiently short to neglect population relaxation during this period. Working in this impulsive limit allows for the signal field to be proportional to the real part of the third-order nonlinear response function [Eq. (15)] and implies that $\tau_n' = \tau_n$. Finally, we do not consider the orientational response function (Y_{IJKL}^{abcd}) or vibrational electrical anharmonicity here.

The energies of the vibrational eigenstates in both electronic states are obtained by diagonalization of $H_{vibronic}$. In general, $H_{vibronic}$ cannot be block-diagonalized since the linear, quadratic, and cubic perturbations result in the coupling of manifolds with differing numbers of quanta. In principle, the system eigenstates are determined by obtaining the eigenvalues and eigenvectors of $H_{vibronic}$ with infinite size. In practice, this is achieved by choosing a matrix size large enough to obtain numerical convergence of the lowest five vibrational states in both electronic manifolds. For these simulations, $H_{vibronic}$ was expanded to 50 vibrational quanta. The transformation between the local mode basis and the eigenstate basis is defined by $H'_{vibronic} = T^{-1}H_{vibronic}T$, where $H'_{vibronic}$ is in the eigenstate basis and T is the transformation matrix whose columns are the eigenvectors that represent the contributions of the states in the local mode basis to the eigenstates of the vibronic Hamiltonian. The vibrational transition dipole moments are transformed similarly using T to transform an initially harmonic transition dipole moment matrix.

The $H_{vibronic}$ parameters used in the simulation are given in the corresponding figures below. When coefficients are described as nonzero, their values are as follows: $g_{jjj} = 0.25$

yields a 30 cm^{-1} anharmonicity, $V_j^{(1)} = 1$ reflects an excited state displacement equal to the ground state equilibrium bond length, $V_{j,j}^{(2)} = -0.038$ translates to a 40 cm^{-1} red-shifted vibrational frequency in $|e\rangle$, Herzberg-Teller couplings (non-Condon effects) are included with $\mu_{eg}^{(1)} = 0.15$, and $\lambda = 1.5$ sets the vibrational dephasing in $|e\rangle$ to be 50% faster than in $|g\rangle$. A zeroth-order vibrational frequency $\omega_j{}^0 = 2100$ cm^{-1} and an unperturbed electronic transition frequency $\omega_{eg}^0 = 25\,000$ cm^{-1} are used in all cases. The correlation functions contribute spectral broadening of $\Gamma_{eg,eg} = 200$ cm^{-1}, $\Gamma_{eg,v} = 10$ cm^{-1}, and $\Gamma_{v,v} = 5$ cm^{-1}. In each plot, the linear spectrum for the ω_1 (ω_3) axis is plotted in gray on the top (side) panel, and the ω_3 projection plotted in black on the side panel is obtained by integrating over ω_1 for each ω_3. The $\omega_{electronic}$ axes have been subtracted by the ω_{eg} value calculated by diagonalizing $H_{vibronic}$ to more easily relate peak separation to the vibronic information of interest. To facilitate comparison, the 2D contours in Figs. 5–8 are normalized to the signal of greatest magnitude throughout the series of cases for 2D spectra shown. Thus, all 2D EV spectra are normalized to peak II in Fig. 6(a), and all 2D VE spectra are normalized to peak I in Fig. 8(f). Similarly, the ω_3 projections in 2D EV simulations are normalized to the greatest magnitude signal of Fig. 8 (b, side panel), and the 2D VE ω_3 projections are normalized to Fig. 8 (f, side panel).

The simulations discussed in the remainder of this section demonstrate that 2D EV and 2D VE signals can be observed when one or more of the following is true for a molecular system: (1) there is linear or quadratic vibronic coupling present, (2) the electronic transition dipole moment has nuclear coordinate dependence, and (3) the system displays electronic-state-dependent vibrational dephasing. These molecular phenomena contribute to the 2D signals through the 2D peak positions, amplitudes, and line shapes. We will demonstrate that when condition (1) is fulfilled (i.e., at least $V_j^{(1)} \neq 0$ or $V_{j,j}^{(2)} \neq 0$), the 2D EV and 2D VE signals are least ambiguous and greatest in magnitude.

A. Case 1: Undisplaced, anharmonic oscillator

The simplest case to consider is the one in which no vibronic coupling is present [case 1, Figs. 5(a) and 5(d)]. Here, the potential energy surfaces represented by $H_{vibronic}$ take the form of an undisplaced, anharmonic oscillator where the anharmonicity coefficient is nonzero but the linear and quadratic vibronic coupling coefficients are zero ($g_{jjj} \neq 0$,

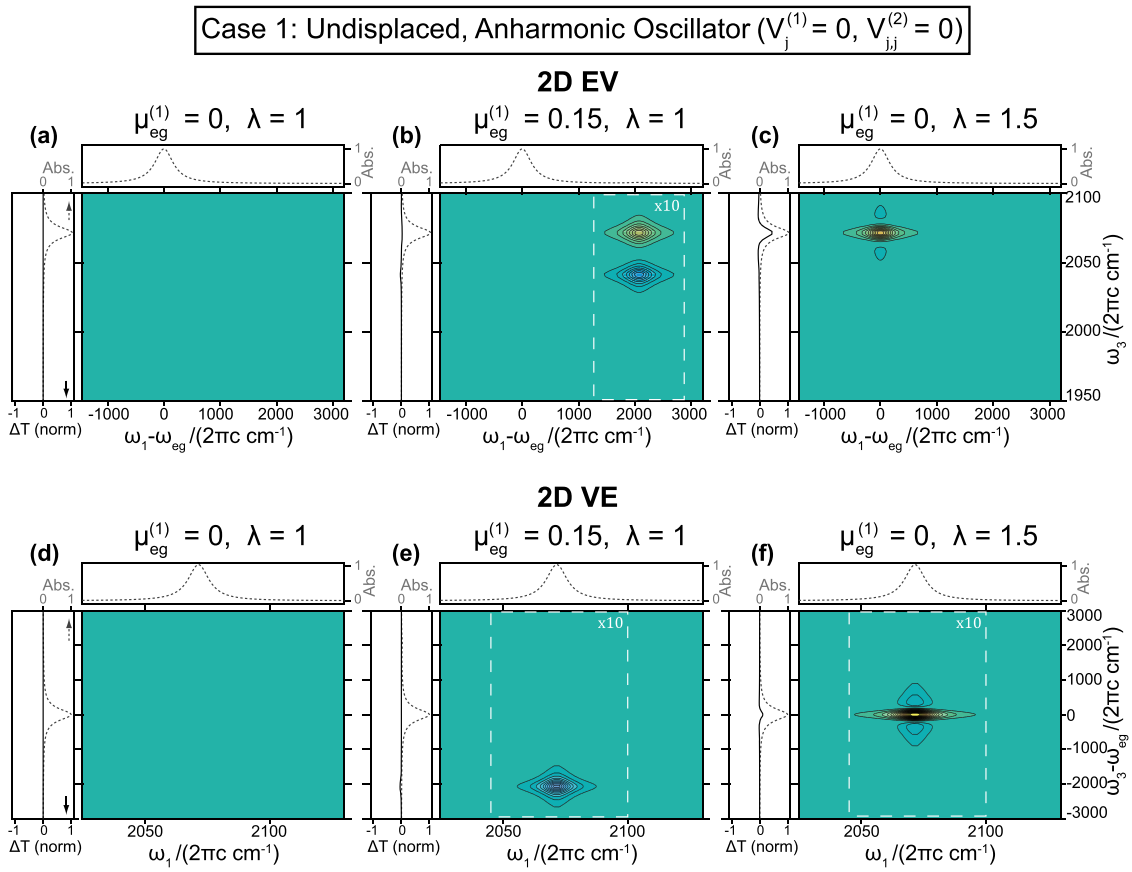

FIG. 5. 2D EV and 2D VE spectral simulations, case 1: the undisplaced anharmonic oscillator. The 2D EV [(a)–(c)] and 2D VE [(d)–(f)] simulations above reflect a system with 30 cm^{-1} anharmonicity and a 2073 cm^{-1} fundamental vibrational frequency in both electronic states. Contour plots (a) and (d) show that there is no signal present in the absence of vibronic coupling ($\mu_{eg}{}^{(1)} = 0$, $\lambda = 1$). Weak or distorted signals from a case 1 system may be observed if non-Condon effects are present [(b) and (e); $\mu_{eg}{}^{(1)} = 0.15$, $\lambda = 1$] or if the system displays electronic-state-dependent vibrational dephasing [(c) and (f); $\mu_{eg}{}^{(1)} = 0$, $\lambda = 1.5$]. The gray plots (top and side panels) are simulated linear spectra (i.e., UV-Vis or FTIR) for the corresponding frequency axis and the black plot (side panels) is an integrated projection onto ω_3 obtained by summing over ω_1. Contours are normalized to the absolute maximum of Fig. 6(a) for 2D EV and Fig. 8(f) for 2D VE; the contours span −1 to 1 with 5% intervals, bleach and emission signals (positive) are yellow, and absorption signals (negative) are blue. The framed 2D regions have been scaled by the factors indicated for emphasis. For relative intensities, see Table I.

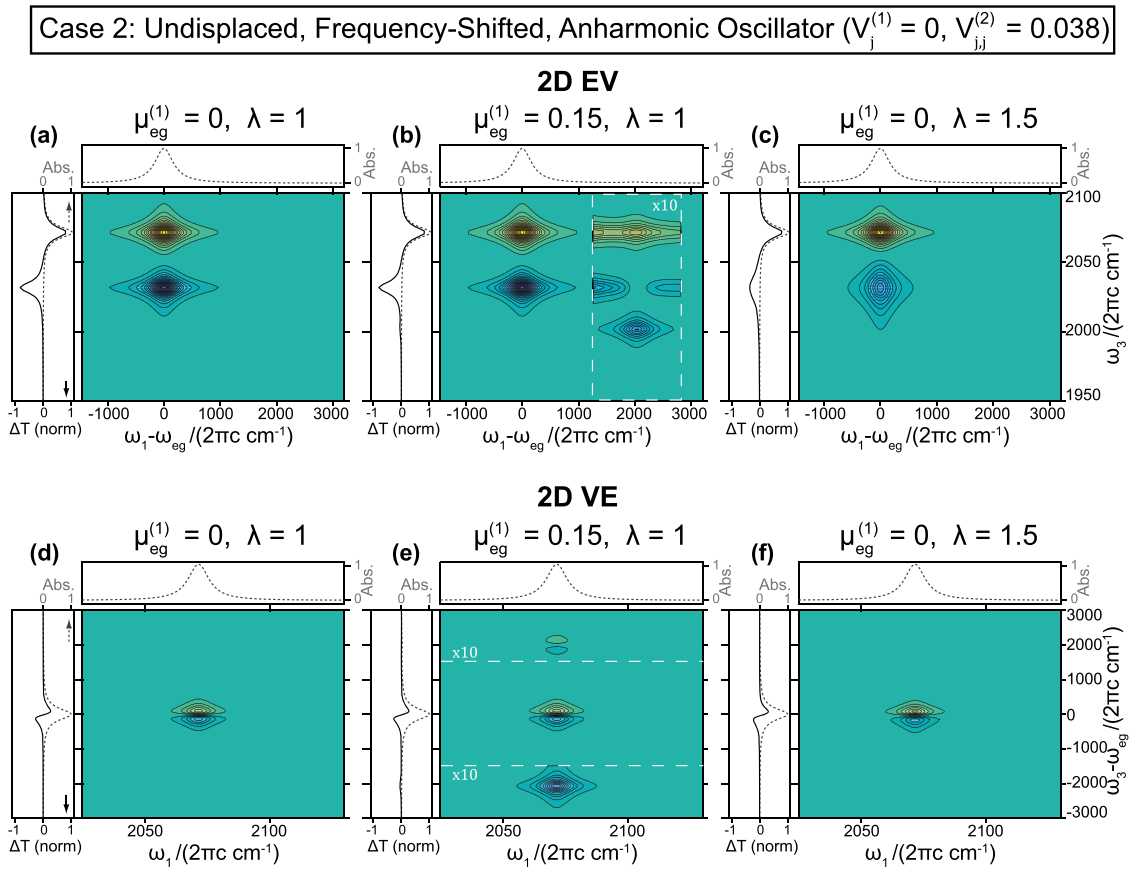

FIG. 6. 2D EV and 2D VE spectral simulations, case 2: the undisplaced, frequency-shifted, anharmonic oscillator. The 2D EV [(a)–(c)] and 2D VE [(d)–(f)] simulations reflect a system with 30 cm^{-1} anharmonicity and a 40 cm^{-1} red-shifted excited state vibration ($\omega_{g,1}$ = 2073 cm^{-1} and $\omega_{e,1'}$ = 2033 cm^{-1}). Contour plots (a) and (d) show that signal is observed when only quadratic vibronic coupling is present ($\mu_{eg}^{(1)}$ = 0, λ = 1). Non-Condon effects are evidenced by small intensity contributions from peaks III-V [(b) and (e); $\mu_{eg}^{(1)}$ = 0.15, λ = 1], and electronic-state-dependent vibrational dephasing effects are observed in the peak II broadening [(c) and (f); $\mu_{eg}^{(1)}$ = 0, λ = 1.5]. The simulated linear spectra (gray plots, top and side panels) are shown for reference. The ω_3 projections (black plots, side panels) are analogous to the pump-probe (or "1D") equivalent signal and provide a comparison between the 2D and pump-probe signals. Contours are normalized to the absolute maximum of Fig. 6(a) for 2D EV and Fig. 8(f) for 2D VE; the contours span −1 to 1 with 5% intervals, bleach and emission signals (positive) are yellow, and absorption signals (negative) are blue. The framed 2D regions have been scaled by the factors indicated for emphasis. For relative intensities, see Table I,

$V_j^{(1)} = 0$, $V_{j,j}^{(2)} = 0$). Additionally, in Figs. 5(a) and 5(d), the Condon approximation is valid ($\mu_{eg}^{(1)} = 0$) and the vibrational dephasing rates in $|e\rangle$ are the same as in $|g\rangle$ ($\lambda = 1$). As is clearly seen in Figs. 5(a) and 5(d), no 2D signal is observed when there is no vibronic coupling present in the system, $\mu_{eg}^{(1)} = 0$, and $\lambda = 1$. Here, the local vibrational mode has the same frequency in the ground and the excited electronic states, and the potential energy surfaces have the same mechanical anharmonicity. Thus, $\omega_{g,1} = \omega_{e,1'}$ and peaks I and II are both centered at the coordinates (ω_{eg},$\omega_{g,1}$) in the 2D EV spectrum and ($\omega_{g,1}$,ω_{eg}) in the 2D VE spectrum. The signal intensities from peaks I and II cancel since the positive signal from the GSB pathways $\left(D_{R,I}^{EV}, D_{NR,I}^{EV}; D_{R,I}^{VE}, D_{NR,I}^{VE}\right)$ and the negative signal from the ESA pathways $\left(D_{R,II}^{EV}, D_{NR,II}^{EV}; D_{R,II}^{VE}, D_{NR,II}^{VE}\right)$ overlap; complete cancellation occurs because the signal amplitudes are equal in magnitude and the line shapes are the same leaving no signal to be observed. The equivalence of the peak I and II amplitudes is due to the equivalent magnitudes of the transition dipole moments involved in the $\mathbf{k_3}$ interaction since both peaks utilize the same transition dipole moment during excitation. Therefore, the absence of 2D EV signals in Fig. 5(a) conveys that $\mu^{g0,g1} = \mu^{e0',e1'}$ in the molecular system, whereas the 2D VE spectrum in Fig. 5(d) suggests that $\mu^{g0,e0'} = \mu^{g1,e1'}$. Additionally, the absence of excited state equilibrium displacement $\left(V_j^{(1)} = 0\right)$ results in negligible Franck-Condon factors for the electronic transitions resonant with $\omega_{electronic} = \omega_{eg} \pm \omega_{e,1'}$ rendering peaks III, IV, and V unobservable in 2D EV and 2D VE. In contrast to other multidimensional spectroscopies such as 2D IR, mechanical anharmonicity in the system is not a sufficient condition to yield 2D EV or 2D VE signals.

2D EV and 2D VE signals may still be observed if $\mu_{eg}^{(1)} \neq 0$, as shown in Figs. 5(b) and 5(e). Non-Condon effects manifest themselves in 2D EV and 2D VE spectra through additional peak intensity contributions. This is most easily seen for 2D EV in Fig. 5(b) and for 2D VE in Fig. 5(e) where the framed 2D spectral regions have been scaled by a factor of 10 to show the non-Condon intensity contributions, the ω_3 projections (black lines in side panels) relate the magnitude of the non-Condon signal contributions. The 2D EV non-Condon signatures in the absence of vibronic coupling only allow peaks III, IV, and V to appear. Interestingly, the only 2D VE non-Condon signature

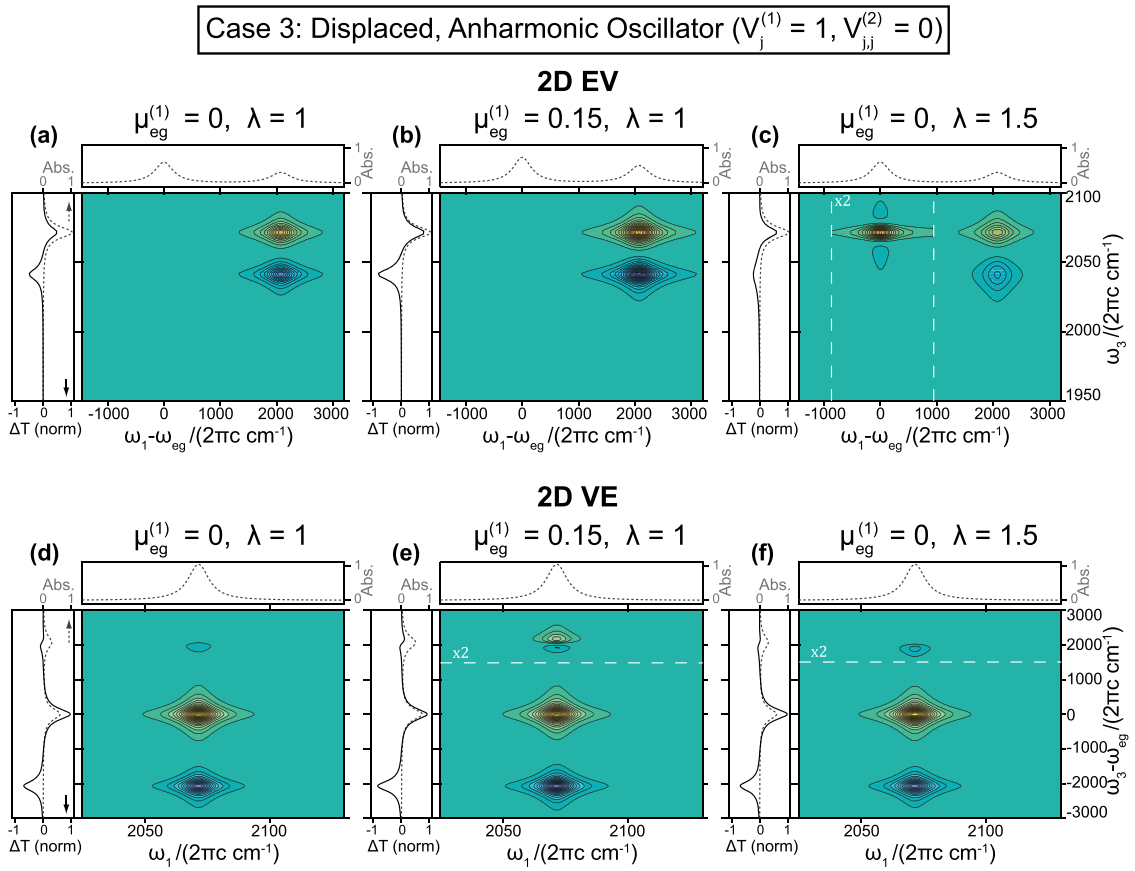

FIG. 7. 2D EV and 2D VE spectral simulations, case 3: the displaced anharmonic oscillator. The 2D EV [(a)–(c)] and 2D VE [(d)–(f)] simulations reflect a system with 30 cm^{-1} anharmonicity, an excited state geometry displacement equal to the ground state equilibrium distance, and a 2073 cm^{-1} fundamental vibrational frequency in both electronic states. Contour plots (a) and (d) show that a signal is observed when only linear vibronic coupling is present ($\mu_{eg}^{(1)} = 0$, λ = 1). Non-Condon effects are evidenced by small intensity contributions to peaks III-V [(b) and (e); $\mu_{eg}^{(1)}$ = 0.15, λ = 1], and electronic-state-dependent vibrational dephasing effects are observed in broadened 2D EV peaks II, IV, and V and broadened 2D VE peaks II and IV [(c) and (f); $\mu_{eg}^{(1)} = 0$, λ = 1.5]. The simulated linear spectra (gray plots, top and side panels) are shown for reference. The ω_3 projections (black plots, side panels) provide comparison between the 2D and pump-probe signals for the respective techniques. Contours are normalized to the absolute maximum of Fig. 6(a) for 2D EV and Fig. 8(f) for 2D VE; the contours span −1 to 1 with 5% intervals, bleach and emission signals (positive) are yellow, and absorption signals (negative) are blue. The framed 2D regions have been scaled by the factors indicated for emphasis. For relative intensities, see Table I.

in this case is peak V because there is no oppositely signed peak pair to negate the non-Condon intensity contribution. Generally, the non-Condon intensity contributions are a more significant addition for transitions with small Franck-Condon factors (e.g., transitions resonant with $\omega_{electronic} = \omega_{eg} + \omega_{e,1'}$ when $V_j^{(1)} \approx 0$). Within the Condon approximation ($\mu_{eg}^{(1)} = 0$), the peak intensities are scaled only by the appropriate Franck-Condon factor for the $|g, v\rangle \rightarrow |e, v'\rangle$ transition. The ratio of peak intensities for signals arising from different electronic transitions should scale with the ratio of the corresponding Franck-Condon factors. The ratio of peak intensities will deviate from the ratio of Franck-Condon factors in the presence of non-Condon effects.

It is also possible to observe 2D EV and 2D VE signals if the line shapes of the positive and negative signals are different, which occur when the vibrational dephasing rates in the two electronic states are unequal [$\lambda \neq 1$, see Figs. 5(c) and 5(f)]. The magnitudes of these signals will depend on how different the vibrational dephasing rates are; a faster dephasing rate yields a broadened peak and imperfect cancellation with an accompanying peak of opposite sign. Lacking any quadratic vibronic coupling to separate the oppositely signed peaks, convoluted peak shapes such as those in Figs. 5(c) and 5(f) may be observed.

B. Case 2: Undisplaced, frequency-shifted, anharmonic oscillator

We next model a case in which vibronic coupling gives rise to 2D EV and 2D VE signals by shifting the frequency of the vibrational mode upon electronic excitation while $\mu_{eg}^{(1)} = 0$ and $\lambda = 1$. This undisplaced, frequency-shifted, anharmonic oscillator [case 2, Figs. 6(a) and 6(d)] potential is modeled by $H_{vibronic}$ with a nonzero anharmonicity coefficient and quadratic vibronic coupling ($g_{jjj} \neq 0$, $V_j^{(1)} = 0$, $V_{j,j}^{(2)} \neq 0$). In both techniques, the GSB (peak I) and the ESA (peak II) peaks still have the same magnitude and sign as in case 1, but the quadratic vibronic coupling separates the two signals along ω_3 because $\omega_{g,1} \neq \omega_{e,1'}$. As in case 1, peaks III, IV, and V are unobserved since $V_j^{(1)} = 0$. The two peaks seen in 2D EV for case 2 [Fig. 6(a)] originate from the first vibrational transition in two separate electronic manifolds. Thus, the direct comparison of the time-dependent positions, line shapes, and amplitudes of these 2D EV signals highlights the differences in the

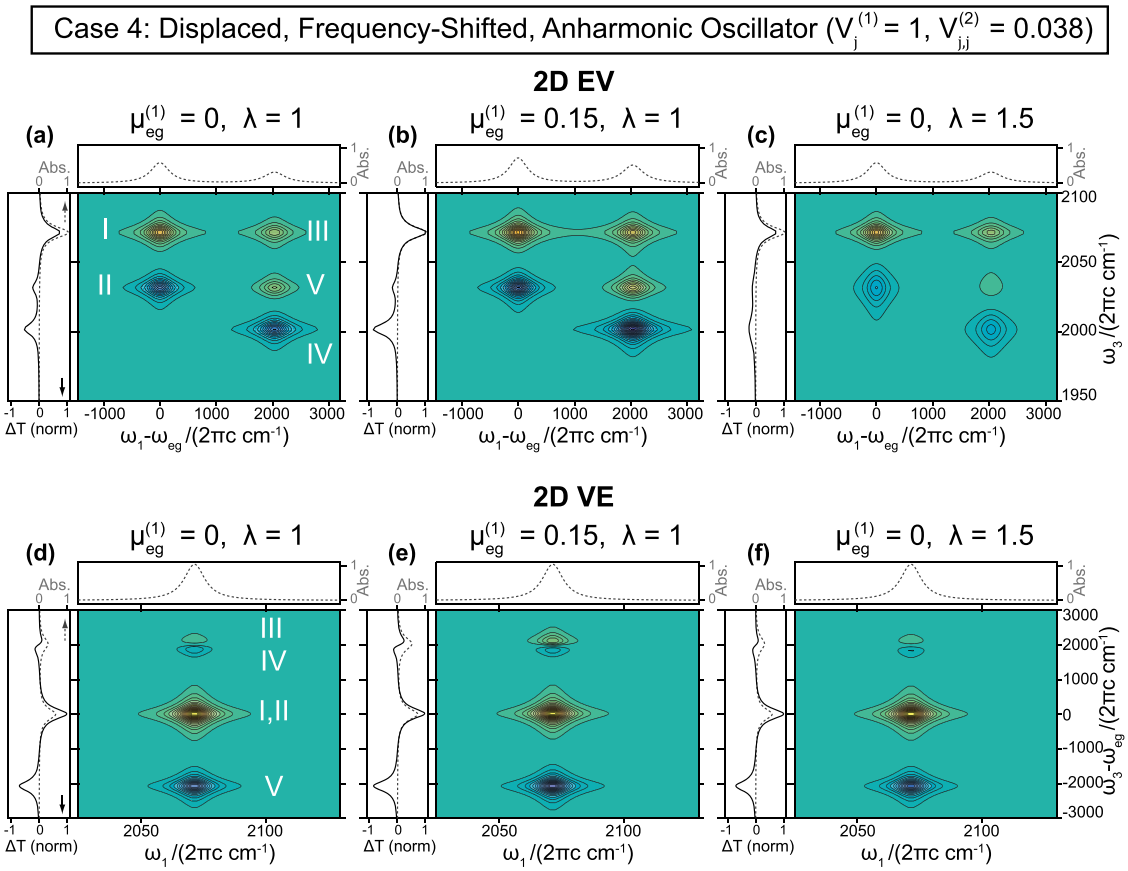

FIG. 8. 2D EV and 2D VE spectral simulations, case 4: the displaced, frequency-shifted, anharmonic oscillator. The 2D EV [(a)–(c)] and 2D VE [(d)–(f)] simulations reflect a system with 30 cm^{-1} anharmonicity, an excited state geometry displacement equal to the ground state equilibrium distance, and a 40 cm^{-1} red-shifted excited state vibrational frequency ($\omega_{g,1}$ = 2073 cm^{-1} and $\omega_{e,1'}$ = 2033 cm^{-1}). Contour plots (a) and (d) show that a signal is observed when both linear and quadratic vibronic couplings are present ($\mu_{eg}^{(1)} = 0$ and $\lambda = 1$). Non-Condon effects are evidenced by small intensity contributions to all peaks in varying proportions [(b) and (e); $\mu_{eg}^{(1)} = 0.15$, $\lambda = 1$], and electronic-state-dependent vibrational dephasing effects are observed in broadened 2D EV peaks II, IV, and V and broadened 2D VE peaks II and IV [(c) and (f); $\mu_{eg}^{(1)} = 0$, $\lambda = 1.5$]. The simulated linear spectra (gray plots, top and side panels) are shown for reference. The 2D EV ω_3 projections (black plots, side panels) in this case highlight the convoluted nature of the 1D ("transient-IR") signal by comparison with the 2D EV signal. Contours are normalized to the absolute maximum of Fig. 6(a) for 2D EV and Fig. 8(f) for 2D VE; the contours span −1 to 1 with 5% intervals, bleach and emission signals (positive) are yellow, and absorption signals (negative) are blue. For relative intensities, see Table I.

potential energy surfaces of the ground and excited electronic states. The comparison of signals for the same vibrational transition in either electronic manifold is a distinct advantage of 2D EV spectroscopy. The 2D VE peaks in this case arise from a difference in electronic energy gaps for the resonant transitions $|g,0\rangle \rightarrow |e,0'\rangle$ and $|g,1\rangle \rightarrow |e,1'\rangle$. In principle, the frequency separation of peaks I and II in the ω_3 dimension for both techniques is represented by $\Delta_{eg} = \omega_{e,1'} - \omega_{g,1}$. However, the resolution of the true Δ_{eg} from a 2D EV or 2D VE spectrum depends on the relative magnitudes of Δ_{eg} and the 2D peak linewidths in the ω_3 dimension. Generally, 2D EV spectra provide higher resolution of Δ_{eg} since the probed vibrations have narrower linewidths than the electronic transitions probed in 2D VE. Using second-order stationary perturbation theory (see Sec. SI.3 of the supplementary material), we can show that Δ_{eg} directly reports on $V_{j,j}^{(2)}$ through the following relation:

$$\Delta_{eg} = \frac{\omega_j{}^0}{2\pi c}\left(\frac{V_{j,j}^{(2)}}{2} - \frac{\left(V_{j,j}^{(2)}\right)^2}{8}\right), \tag{32}$$

where c is the speed of light. For a more complex system involving two or more coupled vibrational modes that may have different anharmonicities, Δ_{eg} will include additional terms from the Hamiltonian. This case shows that quadratic vibronic coupling is a sufficient condition for the observation of 2D EV and 2D VE signals.

The intensity contributions from the presence of non-Condon effects allow for peaks III, IV, and V to be weakly observed [Figs. 6(b) and 6(e)], in addition to peaks I and II. These non-Condon signal intensities are an order of magnitude less than signals present within the Condon approximation. Notably, the fact that $V_{j,j}^{(2)} \neq 0$ allows for 2D VE peaks III and IV to be weakly observed through non-Condon intensity contributions in this case, whereas in case 1, these peaks were still unobservable. Similarly, the positive 2D EV peaks III and V are separated by Δ_{eg} and they appear as weak shoulder features on the tails of peaks I and II, respectively. Hence, the positive intensity of peak V (an ESE pathway) cancels the tail of the negative intensity of peak II, as shown in Fig. 6(b). The relative magnitudes of these non-Condon intensity contributions are shown in the ω_3 projections [black lines in

side panels, Figs. 5(b) and 5(e)] and in the simulated linear electronic absorption spectrum [gray line in top panel, Fig. 5(b)].

The presence of electronic-state-dependent vibrational dephasing ($\lambda \neq 1$) is now very clearly observed through the difference in line shapes between peaks I and II in both 2D EV and 2D VE [Figs. 6(c) and 6(f)]. The broadened ESA peaks reflect faster vibrational dephasing for a molecule in the excited electronic state when compared to the ground electronic state vibrational dephasing rate. In contrast to the previous case, the quadratic vibronic coupling results in the separation of these peaks with different line shapes which allows for a less ambiguous assessment of the electronic-state-dependent vibrational dephasing.

The ω_3 projections in the side panels shown in all of the simulations are the pump-probe analogs to the 2D EV or 2D VE technique. These can be considered the corresponding "1D" signals for either EV (commonly referred to as "transient-IR absorption") or VE. In case 2, where quadratic vibronic coupling has shifted the excited state vibrational frequency, the transient-IR signal and the 2D EV signal both contain sufficient information to extract Δ_{eg}; the new information obtained in 2D EV comes from analyzing and comparing the time dependent 2D line shapes of peaks I and II. The presence of non-Condon effects may also be detected in the transient-IR signal, albeit very weakly. However, since the transient-IR signal lacks ω_1 resolution, the assignment of this intensity contribution to a non-Condon effect is ambiguous because it cannot be correlated with $\omega_{electronic} = \omega_{eg} + \omega_{e,1'}$ excitation, while in 2D EV, the correlation is explicit.

C. Case 3: Displaced, anharmonic oscillator

In case 3, only linear vibronic coupling is present in the system of anharmonic oscillators ($g_{jjj} \neq 0$, $V_j^{(1)} \neq 0$, $V_{j,j}^{(2)} = 0$) and initially it is assumed that $\mu_{eg}^{(1)} = 0$ and $\lambda = 1$ [Figs. 7(a) and 7(d)]. In this case, the vibrational mode oscillates about a different equilibrium position in the excited state due to linear vibronic coupling. The Franck-Condon factors for the vibronic transitions yielding peaks III, IV, and V are non-negligible and so appreciable intensity from these peaks is observed. The 2D EV signal observed [Fig. 7(a)] is specifically from the pathways which include resonant excitation with $\omega_{electronic} = \omega_{eg} + \omega_{e,1'}$. There are no intensity contributions from vibronic pathways that are excited with a frequency $\omega_{electronic} = \omega_{eg}$ because $\omega_{g,1} = \omega_{e,1'}$, thus peaks I and II cancel. For the same reason, peak III (GSB) and peak V (ESE) are exactly overlapped in the 2D EV spectrum and only two features are observed overall. However, peaks III and V have the same sign and so their amplitudes add together instead of canceling. The negative ESA signal (peak IV) appears at the frequency of the second vibrational transition in the excited electronic state ($\omega_{e,2'}$), and it is separated in the $\omega_{vibrational}$ dimension by the frequency difference between $\omega_{e,1'}$ and $\omega_{e,2'}$. This frequency difference, $\Delta_{2',1'} = \omega_{e,1'} - \omega_{e,2'}$, reflects the anharmonicity of the excited state potential energy surface and is expressed in terms of the anharmonic coefficient g_{jjj} (as shown in Sec. SI.3 of the supplementary material): $\Delta_{2',1'} = \left(\omega_j^0/2\pi c\right)\left(15g_{jjj}^2/2\right)$. Interestingly, the positive signal for a molecular system modeled in case 3 [Fig. 7(a)] contains contributions from the equivalent vibrational transition in two different electronic states. Thus, the time-dependent position, line shape, and amplitude of this positive 2D EV feature result from the convolution of the structural dynamics on both potential energy surfaces. In contrast to the 2D EV spectrum, the 2D VE signal observed in case 3 [Fig. 7(d)] contains contributions from peaks I and II because the amplitudes of these peaks are not equal when $V_j^{(1)} \neq 0$. However, since $V_{j,j}^{(2)} = 0$, there will never be more than one peak observed at $\omega_3 = \omega_{eg}$ in case 3. The positive signal at $\omega_3 = \omega_{eg}$ in Fig. 7(d) demonstrates that $|\langle g,0|e,0'\rangle| > |\langle g,1|e,1'\rangle|$ when $V_j^{(1)} = 1$, and so the positive GSB signal dominates. Similarly, the overall negative signal at $\omega_3 \cong \omega_{eg} + \omega_{e,1'}$ suggests that the Franck-Condon factor corresponding to peak IV has a larger magnitude than the Franck-Condon factor for peak III. More important, however, is the fact that the frequency separation between peaks III and IV is $\omega_{eg} + \omega_{e,1'} + \Delta_{eg} - \Delta_{2',1'}$; thus, peaks III and IV do have frequency separation because of the mechanical anharmonicity of the excited state potential energy surface, $\Delta_{2',1'}$, even though $\Delta_{eg} = 0$ in this case. This combination of magnitude differences in Franck-Condon factors when $V_j^{(1)} \neq 0$ and the excited state anharmonicity facilitates the observation of an overall 2D VE signal between peaks III and IV. Overall, case 3 demonstrates that linear vibronic coupling is also a sufficient condition for the observation of 2D EV and 2D VE signals.

The presence of non-Condon effects in case 3 simply enhances the peaks that arise due to linear vibronic coupling in the system. As shown in Fig. 7(b), the intensity of the 2D EV spectral signatures is greater. The signal magnitude enhancement is also seen by comparing the ω_3 projections in Figs. 7(a) and 7(b). While non-Condon intensity contributions to peaks I and II do occur, both of these transition pathways involve the same electronic transition and so the nuclear dependence of this $|g,0\rangle \rightarrow |e,0'\rangle$ excitation is reflected equally in both peaks; thus, peaks I and II still completely cancel. Notably, the 2D VE non-Condon intensity contributions highlight the difference in the nuclear dependence of the different electronic transition dipole moments that contribute to each of the 2D VE peaks. This is demonstrated most clearly by peaks III and IV in Fig. 7(e). In this case, the non-Condon intensity allows both peaks III and IV to be observed with their separation given by $\Delta_{2',1'}$.

When electronic-state-dependent vibrational dephasing is present in a molecular system modeled by case 3, we see different line shapes in Figs. 7(c) and 7(f). In 2D EV, the direct comparison of vibrational dephasing dynamics in the two electronic states is convoluted because peaks III and V are overlapped, as are peaks I and II. However, since peaks III and V are both positive, identifying dephasing dynamics specific to a vibration in one electronic state is ambiguous. Provided that the excited state anharmonicity is large enough to spectrally separate peak IV from peaks III and V, then it is still possible to analyze excited state dephasing information in isolation. The line shapes in 2D VE will be less sensitive to excited-state-dependent vibrational dephasing due to the inherently large width of the probed electronic

transitions and the λ-dependence of the 2D VE dephasing functions.

It is important to highlight the difference in interpreting the transient-IR signal and the 2D EV signal for this case, in particular. A usual interpretation of transient-IR signals is in the context of excited state frequency shifting of a vibrational mode. However, as is shown in Figure 7 [(a)–(c), contours], the ω_3 frequency separation of the positive and negative signals is only due to the excited state anharmonicity. There is no quadratic vibronic coupling in case 3, and the mechanical anharmonicities are the same in $|e\rangle$ and $|g\rangle$; therefore, $\Delta_{eg} = 0$. With only the transient-IR signal to conclude about the differences of the molecular system in the ground and excited electronic states, it would be reasonable—but incorrect—to conclude that the measured frequency separation between the positive and negative peaks is the difference in vibrational frequency between the two electronic states. In fact, this frequency separation would be the excited state mechanical anharmonicity.

D. Case 4: Displaced, frequency-shifted, anharmonic oscillator

The final case considers a system in which all the parameters in $H_{vibronic}$ are nonzero ($g_{jjj} \neq 0$, $V_j^{(1)} \neq 0$, $V_{j,j}^{(2)} \neq 0$). Here, the potential energy surfaces take the form of displaced, frequency-shifted, anharmonic oscillators. For 2D EV spectra of molecular systems modeled by case 4 [Fig. 8(a)], peaks I-V are observable, and Δ_{eg} and $\Delta_{2',1'}$ can be obtained directly from the 2D EV spectrum. The presence of quadratic vibronic coupling uniformly affects the $\omega_{vibrational}$ peak separation of vibrations in $|e\rangle$ (peaks II, IV, and V) and vibrations in $|g\rangle$ (peaks I and III). Notably, this results in the separation of the GSB (III) and the ESE (V) signals that were convolved in case 3. The 2D VE spectrum for case 4 [Fig. 8(d)] also contains contributions from all vibronic transition pathways, but only four spectral signatures are observed because the positive signal in peak I eclipses the negative signal from peak II. This occurs for the same reasons described above in case 3 [Fig. 7(d)].

The non-Condon intensity contributions in case 4 enhance all of the peaks, and the magnitude of the contributions reflect the nuclear dependence of a particular vibronic transition. For vibronic transitions with relatively large Franck-Condon factors, a first order non-Condon ($\mu_{eg}^{(1)}$) contribution will be comparably less noticeable than for transitions with smaller Franck-Condon factors. In 2D EV, the maximum amplitude comparison between peaks I and III will include the Franck-Condon factors and any non-Condon effects. If the Franck-Condon factors for these transitions are obtained using computational methods or measured independently, then a ratio of the measured amplitudes of 2D EV peaks I and III can be used to extract the magnitude of the non-Condon intensity contributions. The non-Condon intensity contributions in 2D VE are most obvious by comparing peaks III and IV, for the same reasons described for case 3 above. However, $\Delta_{eg} \neq 0$ in case 4, so peaks III and IV are further separated and have greater observed amplitude.

In 2D EV, the electronic-state-dependent vibrational dephasing results in the line shapes of the excited state vibrational signatures (II, IV, and V) having broadened features along ω_3 [Fig. 8(c)]. Since all of these features are spectrally resolved, information about vibrational-level-dependent dephasing in the excited electronic state can be extracted by comparing τ_2-dependent line shapes of peaks IV and V in addition to electronic-state-dependent vibrational dephasing information accessible by comparing peaks I and II.

In this case, where peaks I-V contribute appreciable intensity to the 2D EV spectrum, the transient-IR signals will be increasingly complex [Figs. 8(a)–8(c)]. For example, since peaks II and V are opposite in sign and have the same ω_3 coordinate, the negative transient-IR signal that should be used to extract Δ_{eg} will be diminished. In this case, the minimum in the transient-IR signal corresponds to the intensity contributions from peak IV at $\omega_3 = \omega_{e,2'}$, which is only realized by resolving the excitation frequency axis in the 2D EV spectrum. The assessment of Δ_{eg} from the transient-IR signal alone should be approached with caution.

We briefly discuss how the 2D EV and 2D VE signals in Figs. 8(a) and 8(d) would be different for the case of the displaced harmonic oscillator (DHO) model,[46] commonly used to simulate 2D ES signals. The DHO model is approximated by $H_{vibronic}$ [Eqs. (1)–(4)], when $g_{jjj} = 0$. If the oscillators in the DHO model have the same vibrational frequency in both electronic states and they are harmonic, then $\Delta_{eg} = 0$ and $\Delta_{2',1'} = 0$. In 2D EV, all the oppositely signed signals would emit at the same frequency. Therefore, 2D EV signals will not be observed for a DHO system that lacks quadratic vibronic coupling. We would still observe 2D EV signals if the vibrational dynamics were dependent on the electronic state. If the vibrational frequency is different in the ground and excited electronic states for the DHO model ($\Delta_{eg} \neq 0$), 2D EV signals will be observed. However, peaks IV and V will be overlapped (since $\Delta_{2',1'} = 0$) and their amplitudes will incompletely cancel due to the different magnitudes of peaks IV and V. In contrast, 2D VE signals arising from the DHO model will always be observed because the displacement of the ground and electronic states results in different amplitudes of the oppositely signed peaks in the 2D VE peak pairs (e.g., peaks I and II).

V. SELECTION RULES FOR 2D EV AND 2D VE SPECTROSCOPIES

The systematic investigation of simulated 2D EV and 2D VE spectra in Sec. IV suggests that these 2D spectroscopies are subject to these three general selection rules: (1) the presence of vibronic coupling in the system represented by at least one nonzero vibronic coupling coefficient ($V_j^{(1)} \neq 0$ or $V_{j,j}^{(2)} \neq 0$), (2) the electronic transition dipole moment is dependent on the nuclear coordinates (i.e., the Herzberg-Teller coupling or higher order non-Condon effects are appreciable), and (3) the system displays electronic-state-dependent vibrational dephasing dynamics. These selection rules relate the propensity for molecular systems to display signals when studied with 2D EV or 2D VE spectroscopies through the measured peak positions, amplitudes, and line shapes. A concise summary of the information presented in the

TABLE I. This table summarizes some of the information conveyed in the series of 2D EV and 2D VE simulations shown in Figs. 5–8. The following is organized by grouping cases 1-4 for three combinations of the $\mu_{eg}^{(1)}$ and λ parameters. The first four rows show cases 1-4 under the Condon approximation and with no electronic-state-dependent vibrational dephasing ($\mu_{eg}^{(1)} = 0$, $\lambda = 1$); rows 5-8 show the influence of non-Condon effects on all cases ($\mu_{eg}^{(1)} = 0.15$, $\lambda = 1$); rows 8-12 show the effects of electronic-state-dependent vibrational dephasing for all four cases ($\mu_{eg}^{(1)} = 0$, $\lambda = 1.5$); and the last row (simulation not shown) shows a case 4 system where all simulation parameters are nonzero ($\mu_{eg}^{(1)} = 0.5$, $\lambda = 1.5$). Each row corresponds to a set of conditions used to simulate 2D EV and 2D VE spectra (excluding the last row); the absolute maximum peak intensities (I_{max}) for 2D EV and 2D VE simulations are listed and normalized for comparison. The peak with the greatest magnitude and the figure in which the simulation is shown are given for referencing the simulations shown earlier in the text.

$V_j^{(1)}$	$V_{j,j}^{(2)}$	$\mu_{eg}^{(1)}$	λ	I_{max}^{EV}	[peak, figure]	I_{max}^{VE}	[peak, figure]
0	0	0	1	0	[-, 5(a)]	0	[-, 5(d)]
0	–0.038	0	1	1.000	[II, 6(a)]	0.273	[I/II, 6(d)]
1	0	0	1	0.535	[IV, 7(a)]	0.969	[I, 7(d)]
1	–0.038	0	1	0.581	[II, 8(a)]	0.986	[I, 8(d)]
0	0	0.15	1	0.040	[II, 5(b)]	0.052	[V, 5(e)]
0	–0.038	0.15	1	0.999	[II, 6(b)]	0.274	[II, 6(e)]
1	0	0.15	1	0.886	[IV, 7(b)]	0.918	[I, 7(e)]
1	–0.038	0.15	1	0.918	[IV, 8(b)]	0.976	[I, 8(e)]
0	0	0	1.5	0.535	[I, 5(c)]	0.113	[I, 5(f)]
0	–0.038	0	1.5	0.955	[I, 6(c)]	0.310	[I, 6(f)]
1	0	0	1.5	0.342	[III/IV, 7(c)]	0.985	[I, 7(f)]
1	–0.038	0	1.5	0.567	[I, 8(c)]	0.998	[I, 8(f)]
1	–0.038	0.15	1.5	0.701	[I, -]	1.000	[I, -]

simulations (Figs. 5–8) is given in Table I to highlight general trends in 2D EV and 2D VE signals. This information is also useful to compare the sensitivities of 2D EV and 2D VE spectroscopies to different types of vibronic molecular phenomena.

The signals observed in 2D EV spectroscopy are greatest in magnitude when the system only has quadratic vibronic coupling ($V_{j,j}^{(2)} \neq 0$, case 2). For the cases where linear vibronic coupling is present, the signal is still greater when quadratic vibronic coupling is also present ($V_j^{(1)} \neq 0$, $V_{j,j}^{(2)} \neq 0$, case 4). The simulations show that different spectral signatures characterize the different cases, but the magnitudes of these signals reflect the sensitivity of the technique to various conditions of molecular vibronic coupling. Thus, while 2D EV spectroscopy is sensitive to both linear and quadratic vibronic couplings, it appears to be more sensitive to quadratic vibronic coupling effects. Herzberg-Teller coupling effects are more noticeable in 2D EV spectra when there is already some degree of excited state displacement present in the system, which is expected from a system with stronger vibronic coupling. Finally, 2D EV spectroscopy is particularly sensitive to electronic-state-dependent vibrational dephasing dynamics, especially when $V_{j,j}^{(2)} \neq 0$. Since spectral signatures from vibrations in both electronic states appear in 2D EV, the line shapes that reflect these dephasing dynamics can be analyzed for each electronic state for direct comparison.

The signals observed in 2D VE spectroscopy appear to be less sensitive to quadratic vibronic coupling and more sensitive to linear vibronic coupling. As seen from Table I, the signals are overwhelmingly larger when $V_j^{(1)} \neq 0$ (cases 3 and 4) than when $V_j^{(1)} = 0$ (cases 1 and 2). The broad linewidths of the probed electronic transitions result in extensive overlapping features in 2D VE spectra. Therefore, the observed peak is far more dependent on the relative amplitudes between competing spectral features of differing sign and line shape than on peak separation. 2D VE has a unique sensitivity to the nuclear dependence of different vibronic transitions because the 2D VE pathways sample more electronic transition dipole moments within the molecular system than in 2D EV. Thus, Herzberg-Teller coupling effects result in non-trivial amplitude comparisons of oppositely signed spectrally congested features.

The propensities for observing 2D EV and 2D VE signals follow for the case in which all simulation parameters are non-zero (Table I, last row), which may be a more realistic case for a molecular system. In 2D EV, the presence of Herzberg-Teller coupling effects increases the observed intensities overall with varying proportions, but the presence of electronic-state-dependent vibrational dephasing disperses the excited state vibrational spectral intensity of the ESA (peak IV) leaving the GSB (peak I) feature with the greatest magnitude. The feature of the greatest magnitude does not change in 2D VE because Herzberg-Teller effects and the excited state vibrational dephasing both contribute to enhancing the positive amplitude of peak I, and so this feature still dominates the spectrum.

VI. DISCUSSION

In 2D EV and 2D VE spectroscopies, the complexity of the spectral and dynamical signatures can increase depending on the accessible transitions during the field-matter interactions. As spectrally broadened and temporally compressed ultrafast pulses throughout the UV, visible, and infrared regions are implemented in spectroscopic experiments, a discussion of the newly accessible signals in these spectroscopies is warranted.[53] For simplicity, we assume $\tau_2' \geq \tau_p$ and briefly consider the new 2D signals that arise when the electronically resonant field reaches higher vibrational levels in $|e\rangle$ with center frequency $\omega_{electronic} = (\omega_{eg} + \omega_{e,1'}) \pm \omega_{g,1}$ and when the vibrationally resonant field has the spectral bandwidth to excite two quantum transitions: Δv, $\Delta v' = \pm 1, \pm 2$.

If $\omega_{electronic} = (\omega_{eg} + \omega_{e,1'}) \pm \omega_{g,1}$ but $\omega_{vibrational}$ does not have increased bandwidth ($\Delta v, \Delta v' = \pm 1$), six new 2D EV Liouville pathways and four new 2D VE Liouville pathways are allowed when $\mathbf{k_1}$ and $\mathbf{k_2}$ leave the system in a population state during τ_2'. These new 2D EV signals result in three new peaks (a GSB, an ESA, and an ESE), while the new 2D VE signals yield a GSB and an ESA peak pair at the expense of peak V since it would be outside of the probe bandwidth. If the bandwidth of $\omega_{vibrational}$ is octave-spanning and $\omega_{electronic} = \omega_{eg} \pm \omega_{g,1}$, then the only new 2D EV Liouville pathways that evolve in population states during τ_2' emit at vibrational overtone frequencies. In contrast, since $\mathbf{k_1}$ and $\mathbf{k_2}$ are vibrationally resonant in 2D VE, ten new Liouville pathways are accessible to the system that yield a new set of

five fully absorptive features at a higher excitation frequency, $\omega_1 = 2\omega_{g,1}$. The dynamics during the τ_2' delay become complex when $\omega_{vibrational}$ is octave-spanning because the system can evolve in a new set of allowed coherence states during τ_2' in both experiments. Four 2D EV Liouville pathways arise that evolve in single quantum coherence states (either $|e,0'\rangle\langle e,1'|$ or $|g,0\rangle\langle g,1|$) and require a vibrational overtone interaction with $\mathbf{k_3}$ to be detected; we note that the conjugates of these pathways emit at overtone frequencies and so would be exceedingly difficult to detect. There are twelve new 2D VE Liouville pathways that evolve as single quantum coherence states ($|g,0\rangle\langle g,1|$+c.c. and $|g,1\rangle\langle g,2|$+c.c.) during τ_2'; in this case, the conjugate coherence states still emit at fundamental vibrational frequencies and will equally contribute to the observed τ_2' dynamics. The signals from these coherence states will contribute additional—and oscillatory—intensity to peaks that already exist from signals that evolve in population states during τ_2'. Similarly, still more signals arise if $\omega_{electronic} = (\omega_{eg} + \omega_{e,1'}) \pm \omega_{g,1}$ *and* $\omega_{electronic}$ is octave spanning.

A description of the electronic transition dipole moment similar to our approach has been used by Turner and coworkers[54] in three-dimensional electronic spectroscopy (3D ES) to identify Herzberg-Teller signatures through antidiagonal nodal features in 3D ES spectra. Other nonlinear vibrational spectroscopies also have been used to probe couplings between electronic and vibrational motion in molecules that principally involve Raman-active vibrations, such as 2D fifth-order Raman spectroscopy,[55] femtosecond stimulated Raman spectroscopy,[56] 2D resonance Raman spectroscopy,[57] and 4D coherent Raman spectroscopy.[58,59] The 2D spectroscopies discussed in this paper contribute the capability for probing IR-active vibrations that are coupled to electronic degrees of freedom. Thus, 2D EV and 2D VE spectroscopies provide an important avenue toward understanding vibronic couplings involving changes in the dipole moment which complement these nonlinear Raman techniques that describe vibronic couplings involving changes in polarizability. Polarization sensitivity has been used in 2D EV experiments to aid with peak assignments in congested spectra of light harvesting complexes.[19] In principle, a combination of polarization selective 2D EV and 2D VE experiments should yield a rich description of the vibronic coupling present in a system by revealing relative orientations of particular IR-active vibrations with respect to the electronic transition dipole moment. We will explore polarization effects in 2D VE and 2D EV spectroscopies in future studies.

A wealth of microscopic information is conveyed by the dynamic 2D line shapes in multidimensional spectroscopy.[60–65] Static and dynamic correlations measured in 2D IR and 2D ES experiments reflect the microscopic nature and time scales of fluctuations in molecular vibrational and electronic transition energies. There has been recent work on extracting static and dynamic correlations between vibrational and electronic transition frequencies using 2D EV spectroscopy.[21,23] We anticipate that continued studies of time-evolving 2D EV and 2D VE line shapes will describe molecular phenomena such as non-equilibrium solvation,[66] transient structural heterogeneity, and non-Gaussian frequency distributions[67] on coupled vibronic states.

In this paper, we have focused our discussion on a single anharmonic vibrational mode coupled to the ground and the first excited electronic states. Most physical systems of interest will include more than one vibration of interest and more than one excited electronic state. It will be important to extend this work to include a vibronic system with multiple coupled vibrations on multiple electronic states. The framework presented here utilizes adiabatic vibronic eigenstates. In future, we will explore how non-adiabatic effects will manifest themselves in 2D EV and 2D VE spectroscopies.

VII. CONCLUSIONS

A framework for interpreting vibronic coupling signatures of molecular ensembles in 2D EV and 2D VE spectra has been outlined in this paper. The simplest case of a molecular system composed of one anharmonic local vibrational mode and two electronic states has been treated here. A system Hamiltonian is described that uses linear, quadratic, and cubic perturbations to model this simple system of an anharmonic vibration in the ground electronic state that may be displaced and frequency-shifted in the excited electronic state. Notably, our treatment parallels the Herzberg-Teller adiabatic approximation and we show that the nuclear dependence of the electronic transitions can be observed in these 2D spectroscopies. We have described three general selection rules for 2D EV and 2D VE spectroscopies: (1) the presence of molecular vibronic coupling, (2) the nuclear dependence of the electronic transitions, and (3) the system displays electronic-state-dependent vibrational dephasing. These effects manifest themselves in the 2D peak positions, amplitudes, and line shapes. A systematic series of 2D EV and 2D VE spectral simulations generally characterizes the nature and magnitude of signals in systems with varying degrees of vibronic coupling.

SUPPLEMENTARY MATERIAL

See supplementary material for Liouville pathways for a third order nonlinear response tensor, response functions for 2D EV and 2D VE spectroscopies, and second order corrections to energies using stationary perturbation theory.

ACKNOWLEDGMENTS

The development of 2D VE spectroscopy is supported by the U.S. Department of Energy, Office of Science, Office of Basic Energy Sciences under Award No. DE-SC0012450. The development of 2D EV spectroscopy is supported by the National Science Foundation (Grant No. CHE 1565759). J.D.G. is supported by the NSF GRFP, Division of Graduate Education (No. DGE-1256082). M.K. thanks the Camille and Henry Dreyfus Foundation for fellowship support.

APPENDIX A: 2D EV AND 2D VE ENERGY GAP CORRELATION FUNCTIONS

The vibronic transition frequency correlation functions relevant for 2D EV and 2D VE spectroscopy are defined as

$$\begin{aligned}
\zeta_{v,v}(t) &= \left\langle \delta\omega_{g1,g0}(t)\delta\omega_{g1,g0}(0)\right\rangle,\\
\zeta_{v',v'}(t) &= \left\langle \delta\omega_{e1',e0'}(t)\delta\omega_{e1',e0'}(0)\right\rangle,\\
\zeta_{eg,eg}(t) &= \left\langle \delta\omega_{e0',g0}(t)\delta\omega_{e0',g0}(0)\right\rangle,\\
\zeta_{eg,v'}(t) &= \left\langle \delta\omega_{e0',g0}(t)\delta\omega_{e1',e0'}(0)\right\rangle,\\
\zeta_{eg,v}(t) &= \left\langle \delta\omega_{g1,g0}(t)\delta\omega_{e0',g0}(0)\right\rangle,\\
\zeta_{v,v'}(t) &= \left\langle \delta\omega_{g1,g0}(t)\delta\omega_{e1',e0'}(0)\right\rangle.
\end{aligned} \tag{A1}$$

Equations (19)–(21) are obtained by simplifying (A1) using λ [Eq. (18)].

APPENDIX B: NUCLEAR COORDINATE DEPENDENCE OF M_{eg}

As the Condon approximation is relaxed and the Herzberg-Teller coupling terms are included ($\mu_{eg}^{(1)} \neq 0$) in Eq. (9), the nuclear dependence of the electronic transition contributes additional intensity to the 2D EV or 2D VE spectrum. In this case, $\mathbf{M}_{eg}(Q)$ is expressed for a single vibrational mode j,

$$\mathbf{M}_{eg}(Q) = \mu_{eg}^{(0)} \langle g, v | e, v' \rangle + \mu_{eg}^{(1)} \langle g, v | Q_j | e, v' \rangle. \tag{B1}$$

The contributions of the Herzberg-Teller coupling terms to the signal intensity is included phenomenologically through the linear expansion coefficient $\mu_{eg}^{(1)}$, which is a weighting coefficient in a linear combination of vibrational overlap integrals. This may be understood by writing Q_j as a ladder operator that raises (or lowers) the vibrational quantum number in the excited electronic state. With this in mind, the expression in (B1) can be rewritten as

$$\mathbf{M}_{eg}(Q) = \mu_{eg}^{(0)} \langle g, v | e, v' \rangle + \mu_{eg}^{(1)} \langle g, v | e, (v \pm 1)' \rangle. \tag{B2}$$

Since the vibrational eigenstates in each electronic manifold are obtained through diagonalization of H_g and H_e, the values of the vibrational overlap integrals are easily obtained. Thus, the coefficient $\mu_{eg}^{(1)}$ describes the magnitude of the nuclear coordinate dependence of the electronic transition by contributing some character of the $|g, v\rangle \rightarrow |e, (v' \pm 1)\rangle$ transition(s) to the $|g, v\rangle \rightarrow |e, v'\rangle$ transition.

[1] G. D. Scholes, G. R. Fleming, L. X. Chen, A. Aspuru-Guzik, A. Buchleitner, D. F. Coker, G. S. Engel, R. van Grondelle, A. Ishizaki, D. M. Jonas, J. S. Lundeen, J. K. McCusker, S. Mukamel, J. P. Ogilvie, A. Olaya-Castro, M. A. Ratner, F. C. Spano, K. B. Whaley, and X. Zhu, Nature **543**, 647 (2017).
[2] N. Christensson, H. F. Kauffmann, T. Pullerits, and T. Mancal, J. Phys. Chem. B **116**, 7449 (2012).
[3] F. D. Fuller, J. Pan, A. Gelzinis, V. Butkus, S. S. Senlik, D. E. Wilcox, C. F. Yocum, L. Valkunas, D. Abramavicius, and J. P. Ogilvie, Nat. Chem. **6**, 706 (2014).
[4] J. M. Womick and A. M. Moran, J. Phys. Chem. B **115**, 1347 (2011).
[5] V. Tiwari, W. K. Peters, and D. M. Jonas, Proc. Natl. Acad. Sci. U. S. A. **110**, 1203 (2013).
[6] V. P. Singh, M. Westberg, C. Wang, P. D. Dahlberg, T. Gellen, A. T. Gardiner, R. J. Cogdell, and G. S. Engel, J. Chem. Phys. **142**, 212446 (2015).
[7] E. Collini and G. D. Scholes, Science **323**, 369 (2009).
[8] Y. Fujihashi, G. R. Fleming, and A. Ishizaki, J. Chem. Phys. **142**, 212403 (2015).
[9] V. Butkus, L. Valkunas, and D. Abramavicius, J. Chem. Phys. **137**, 044513 (2012).
[10] Y. C. Cheng and G. R. Fleming, J. Phys. Chem. A **112**, 4254 (2008).
[11] P. Goyal, C. A. Schwerdtfeger, A. V. Soudackov, and S. Hammes-Schiffer, J. Phys. Chem. B **119**, 2758 (2015).
[12] P. Goyal, C. A. Schwerdtfeger, A. V. Soudackov, and S. Hammes-Schiffer, J. Phys. Chem. B **120**, 2407 (2016).
[13] A. K. Harshan, T. Yu, A. V. Soudackov, and S. Hammes-Schiffer, J. Am. Chem. Soc. **137**, 13545 (2015).
[14] S. Hu, A. V. Soudackov, S. Hammes-Schiffer, and J. P. Klinman, ACS Catal. **7**, 3569 (2017).
[15] G. F. Manbeck, E. Fujita, and J. J. Concepcion, J. Am. Chem. Soc. **138**, 11536 (2016).
[16] T. A. A. Oliver, N. H. C. Lewis, and G. R. Fleming, Proc. Natl. Acad. Sci. U. S. A. **111**, 10061 (2014).
[17] T. L. Courtney, Z. W. Fox, L. Estergreen, and M. Khalil, J. Chem. Phys. Lett. **6**, 1286 (2015).
[18] T. L. Courtney, Z. W. Fox, K. M. Slenkamp, and M. Khalil, J. Chem. Phys. **143**, 154201 (2015).
[19] N. H. C. Lewis and G. R. Fleming, J. Phys. Chem. Lett. **7**, 831 (2016).
[20] J. D. Gaynor, T. L. Courtney, M. Balasubramanian, and M. Khalil, Opt. Lett. **41**, 2895 (2016).
[21] H. Dong, N. H. C. Lewis, T. A. A. Oliver, and G. R. Fleming, J. Chem. Phys. **142**, 174201 (2015).
[22] N. H. C. Lewis, H. Dong, T. A. A. Oliver, and G. R. Fleming, J. Chem. Phys. **143**, 124203 (2015).
[23] N. H. C. Lewis, H. Dong, T. A. A. Oliver, and G. R. Fleming, J. Chem. Phys. **142**, 174202 (2015).
[24] G. Herzberg and E. Teller, Z. Phys. Chem. B **21**, 410 (1933).
[25] R. L. Fulton and M. Gouterman, J. Chem. Phys. **35**, 1059 (1961).
[26] H. Koppel, W. Domcke, and L. S. Cederbaum, J. Chem. Phys. **74**, 2945 (1981).
[27] T. Holstein, Ann. Phys. **8**, 325 (1959).
[28] G. Capano, T. J. Penfold, U. Rothlisberger, and I. Tavernelli, Chimia **68**, 227 (2014).
[29] Z. Zhao and F. C. Spano, J. Chem. Phys. **122**, 114701 (2005).
[30] D. L. Tonks and J. B. Page, Chem. Phys. Lett. **79**, 247 (1981).
[31] M. H. Cho, J. Chem. Phys. **113**, 7746 (2000).
[32] F. Duschinsky, Acta Physicochim. USSR **7**, 551 (1937).
[33] H. M. Lu and J. B. Page, Chem. Phys. Lett. **131**, 87 (1986).
[34] J. C. Vallet, A. J. Boeglin, J. P. Lavoine, and A. A. Villaeys, Phys. Rev. A **53**, 4508 (1996).
[35] C. Cohen-Tannoudji, B. Diu, and F. Laloe, *Quantum Mechanics* (Wiley-Interscience, Paris, 1977).
[36] G. Herzberg, *Molecular Spectra and Molecular Structure I: Spectra of Diatomic Molecules*, 2nd ed. (D. Van Nostrand Company, Inc., New York, 1950).
[37] J. Y. Sung and R. J. Silbey, J. Chem. Phys. **115**, 9266 (2001).
[38] M. Born and R. Oppenheimer, Ann. Phys. **389**, 457 (1927).
[39] C. J. Ballhausen and A. E. Hansen, Annu. Rev. Phys. Chem. **23**, 15 (1972).
[40] D. C. Harris and M. D. Bertolucci, *Symmetry and Spectroscopy: An Introduction to Vibrational and Electronic Spectroscopy* (Dover, New York, 1989).
[41] J. M. Hollas, *Modern Spectroscopy*, 2nd ed. (John Wiley & Sons, West Sussex, England, 1992).
[42] G. Fischer, *Vibronic Coupling: The Interaction between Electronic and Nuclear Motions* (Academic Press, London, 1984).
[43] T. Azumi and K. Matsuzaki, Photochem. Photobiol. **25**, 315 (1977).
[44] M. H. Cho, J. Chem. Phys. **118**, 3480 (2003).
[45] The Herzberg-Teller adiabatic approximation is obtained by expanding the dynamical electronic wave function in terms of a complete set of static electronic wave functions that reference an equilibrium nuclear configuration. These static electronic wave functions are described within the crude adiabatic approximation and greatly restrict the description of the electronic states. A linear nuclear coordinate dependence of the electronic transition dipole moment is included through the first order term in the expansion in the Herzberg-Teller adiabatic treatment, which relaxes the stringent requires of the crude adiabatic wave functions used in the expansion.
[46] S. Mukamel, *Principles of Nonlinear Optical Spectroscopy* (Oxford University Press, New York, 1995).
[47] P. Hamm and M. T. Zanni, *Concepts and Methods of 2D Infrared Spectroscopy* (Cambridge University Press, Cambridge, UK, 2011).
[48] M. Khalil, N. Demirdoven, and A. Tokmakoff, J. Phys. Chem. A **107**, 5258 (2003).
[49] D. M. Jonas, Annu. Rev. Phys. Chem. **54**, 425 (2003).
[50] O. Golonzka and A. Tokmakoff, J. Chem. Phys. **115**, 297 (2001).
[51] T. A. A. Oliver and G. R. Fleming, J. Phys. Chem. B **119**, 11428 (2015).

[52]M. Khalil and A. Tokmakoff, Chem. Phys. **266**, 213 (2001).
[53]F. V. de A. Camargo, L. Grimmelsmann, H. L. Anderson, S. R. Meech, and I. A. Heisler, Phys. Rev. Lett. **118**, 033001 (2017).
[54]L. A. Bizimana, W. P. Carbery, T. A. Gellen, and D. B. Turner, J. Chem. Phys. **146**, 084311 (2017).
[55]K. D. Rector, A. S. Kwok, C. Ferrante, A. Tokmakoff, C. W. Rella, and M. D. Fayer, J. Chem. Phys. **106**, 10027 (1997).
[56]P. Kukura, D. W. McCamant, and R. A. Mathies, Annu. Rev. Phys. Chem. **58**, 461 (2007).
[57]B. P. Molesky, P. G. Giokas, Z. Guo, and A. M. Moran, J. Chem. Phys. **141**, 114202 (2014).
[58]E. Harel, J. Chem. Phys. **146**, 154201 (2017).
[59]A. P. Spencer, W. O. Hutson, and E. Harel, Nat. Commun. **8**, 14732 (2017).
[60]S. T. Roberts, J. J. Loparo, and A. Tokmakoff, J. Chem. Phys. **125**, 084502 (2006).
[61]H. J. Bakker and J. L. Skinner, Chem. Rev. **110**, 1498 (2009).
[62]K. Kwak, D. E. Rosenfeld, and M. D. Fayer, J. Chem. Phys. **128**, 204505 (2008).
[63]F. Šanda, V. Perlík, C. N. Lincoln, and J. Hauer, J. Phys. Chem. A **119**, 10893 (2015).
[64]W. Zhuang, T. Hayashi, and S. Mukamel, Angew. Chem., Int. Ed. **48**, 3750 (2009).
[65]M. Cho, Chem. Rev. **108**, 1331 (2008).
[66]L. M. Kiefer, J. T. King, and K. J. Kubarych, Acc. Chem. Res. **48**, 1123 (2015).
[67]S. Roy, M. S. Pshenichnikov, and T. L. C. Jansen, J. Phys. Chem. B **115**, 5431 (2011).